MEASUREMENTS OF CIRRUS BACKSCATTER PHASE FUNCTIONS USING A HIGH SPECTRAL RESOLUTION LIDAR

by

Robert E. Holz

A thesis submitted in partial fulfillment of
the requirements for the degree of

(Master of Atmospheric and Oceanic Science)

at the

UNIVERSITY OF WISCONSIN MADISON

2002

Acknowledgments

To begin, I would like to thank my mentor, Dr. Edwin Eloranta. His guidance, perseverance and willingness to teach has made a profound impact on my graduate education and made this thesis possible.

I would also like to thank Professor Steve Ackerman for his excellent feedback, guidance, and moral support. His enthusiasm towards science and great sense of humor continue to amaze me.

I would like to thank Päivi Piironen for the hundreds of hours she spent running the HSRL during 1994. This thesis would not be possible without this data. I would also like to thank Ralph Kuehn for spending many hours explaining the intricacies of how to run the HSRL. Thanks to Joe Garcia for implementing the SQL data base to hold the HSRL data which allowed for quick and efficient access. I would like to thank Jim Hedrick for keeping the mechanical components of the HSRL in great shape.

I would also like to thank my parents for their support during my masters education. It is their guidance that has brought me to this point in my life. The final hero of my Masters education is Christy, my girl friend. Her friendship and support during my masters made it all possible.

This thesis was funded by:

NASA grants NAG5-11449 and NAG5-7572

DOE grant DE-FG02-00ER62968

ABSTRACT

A climatology of cirrus backscatter phase functions measured using the High Spectral Resolution Lidar (HSRL) in Madison, WI is presented. In this thesis, a total of 74 data sessions are included. The study includes rigorous quantitative estimates of measurement uncertainties that demonstrate the reliability of the results.

An important conclusion from this study is that the probability distribution of the measured backscatter phase functions of cirrus clouds has a discrete peak at $\frac{P180}{4\pi} \approx 0.04$. However, the results demonstrate that there can be significant variability, values as large as 0.14 and as small as 0.005 are observed. At large depolarization the results show a positive correlation with depolarization. This result has important implications for single channel lidar measurements which require estimates of the backscatter phase function to make measurement of cloud optical depth. The peak suggests that using a single value for the backscatter phase function is reasonable in the majority of retrievals. If depolarization information is available, varying the backscatter phase function as a function of depolarization may improve the estimate.

TABLE OF CONTENTS

Chapter 1

1 Introduction

An accurate model of the earth's climate requires a detailed knowledge of incoming solar and outgoing terrestrial radiation. A key factor in the energy balance is the influence of cirrus clouds. Satellite observations (Wylie, 1994) show that on average more then 40% of the planet is covered by cirrus. Because cirrus clouds exist in the upper troposphere, they are one of the first modulators of the incoming visible radiation and the final barrier to terrestrial radiation into space.

There is great uncertainty about the effect of cirrus clouds on the planets energy budget. Stephens(1990) showed that the balance is dependent upon the optical depth, height, and crystal size distributions in the clouds. It has been found that cirrus clouds can have a positive or negative impact on the energy balance of the earth depending upon their optical characteristics (Stephens, 1990). Thus, global climate models require accurate measurements of cloud radiative and optical properties. (Stephens, 1990)

The optical properties of cirrus clouds are difficult to measure. They exist high in the atmosphere, are optically thin, and are composed of ice crystals of various sizes, shapes, and water content (Heymsfield, 1990). In order to properly characterize cirrus, measurements must be sensitive to optically thin clouds and be able to resolve vertical variations in the optical properties.

Passive, remote sensing instruments have successfully made global measurements of cirrus cloud cover and have estimated cloud emissivity (Wylie, 1994). However, passive measurements can not resolve vertical variations and often lack the sensitivity to measure optically thin clouds. Active remote sensing instruments such as radar and lidar have greater sensitivity allowing measurements of optically thin clouds and can better resolve vertical variations. They have provided detailed measurements of cirrus cloud reflectance properties (Spinhirne, 1995) and vertically integrated optical depths (Sassen, 2001). However, single channel lidar measurements contain insufficient information to separately determine the scattering cross-section and the extinction cross-section as a function of altitude. The determination of the backscatter and extinction cross-sections requires assumptions regarding their relationship (Klett, 1981). Because this relationship is dependent on the size distributions of the scattering crystals, which are highly variable (Heymsfield, 1984), large errors can result.

The High Spectral Resolution Lidar (HSRL) measures two signals that can be processed to yield separate lidar returns from aerosol and molecular scattering. The separation is possible because the wavelength spectrum of the molecular lidar return is Doppler broadened by the thermal motion of the molecules. As explained in chapter 2.3, separation of molecular and aerosol returns permits the HSRL to measure the extinction and aerosol backscatter cross-sections independently and allows the aerosol backscatter phase function to be computed without prior assumptions.

In this thesis, calibrated HSRL measurements of the backscatter phase function are presented. These measurements are accompanied for the first time with rigorous and quantitative estimates of measurement uncertainties, which demonstrate the reliability of the results. One of the important conclusions from the study is that the probability distribution of the backscatter phase functions of ice clouds has a distinct peak. However, the distribution also shows that for individual days large variability exists. This result has important implications for single channel lidar measurements which need estimates of the backscatter phase function to make measurement of cloud optical depth. The peak suggests that, on average, using a single value for the backscatter phase function for single channel lidar optical depth retrievals will produce reasonable results but using a single backscatter phase function for individual profiles can result in large errors.

C h a p t e r 2

2 Lidar Theory

2.1 Introduction

This chapter will investigate the capabilities of a single channel lidar and the HSRL system. The technique for measuring optical properties such as optical depth, backscatter cross-section and the backscatter phase function will be compared for each instrument.

2.2 The Single Channel Lidar

A traditional lidar has a single channel that detects both molecular and aerosol photons backscattered into the receiver field of view. Single channel lidars are limited because there is not enough information to measure both the atmospheric extinction and backscatter cross-section. This can be investigated using the single channel lidar equation:

$$\frac{dN}{dt}(r) = N_o \frac{cA_r}{2r^2}\left(\beta_a(r)\frac{\mathrm{P_a}(\pi,r)}{4\pi} + \beta_m(r)\frac{3}{8\pi}\right)\exp(-2\int_0^r \beta_e(r')dr') \qquad (2.1)$$

Where the optical depth, τ(r), is defined as

$$\tau(r) = \int_0^r \beta_e(r')dr' \qquad (2.2)$$

And where:

$\frac{dN}{dt}(r)$ = Number of $\frac{\text{photons}}{\text{second}}$ received at range (r)

N_o = Number of transmited photons

c = Speed of light, ms^{-1}

A_r = Collecting area of the reciever, m^2

r = Range to the scattering volume, m

β_a = Aerosol scattering cross section, per unit volume, m^{-1}

β_m = Molecular scattering cross section, per unit volume, m^{-1}

β_e = Extinction cross section, per unit volume , m^{-1}

$\frac{P_a(\pi,r)}{4\pi}$ = Aerosol backscatter phase function, sr^{-1}

$r = \frac{ct}{2}$, m

c = Speed of light, ms^{-1}

t = Time, s

The equation has two unknowns, the backscatter cross-section ($\beta_a(r)\frac{P_a(\pi,r)}{4\pi}$ and the extinction cross-section, but only one measurement at each range. In this arrangement assumptions regarding a relationship between the backscatter cross-section and the extinction cross-section must be made to make measurements of optical depth, extinction, and backscatter cross-section. A common inversion method is the Klett technique (Klett, 1981). The method assumes a power law relationship between the extinction and backscatter cross-section. This method can not be applied to optically thin clouds (optical thickness less than one) and can be unreliable (Hughes, 1985). The power law relationship is not based on atmospheric physical properties.

2.3 HSRL Principles

It is clear from the previous discussion that more information is needed in order to measure the extinction and backscatter cross-section independently. A solution to the problem is to separate the returned signal into the molecular and aerosol backscattered components. This is possible because the molecular spectrum is Doppler broadened due to the thermal motion of the molecules, while much larger and heavier aerosols result in minimal broadening of the returned spectrum. Using a laser tuned to an absorbing narrow band filter, only Doppler broadened molecular scattered photons are transmitted through the filter. With the separation there are now two equations to describe the returned signal given by:

$$\frac{dN_m}{dt}(r) = N_o \frac{cA_r}{2r^2}\beta_m(r)\frac{3}{8\pi}\exp(-2\tau(r))$$
$$\frac{dN_a}{dt}(r) = N_o \frac{cA_r}{2r^2}\beta_a(r)\frac{\mathrm{P_a}(\pi,r)}{4\pi}\exp(-2\tau(r)) \qquad (2.3)$$
$$\text{Where: } \frac{\mathrm{P_m}(\pi,r)}{4\pi} = \frac{3}{8\pi}$$

Where $\frac{dN_m}{dt}(r)$ and $\frac{dN_a}{dt}$ are the number of photons backscattered off molecules and aerosols on to the receiver. The molecular backscatter phase function $\frac{\mathrm{P_m}(\pi,r)}{4\pi} = \frac{3}{8\pi}$ is calculated from Raleigh scattering theory. With the addition of a density profile the molecular scattering cross-section is described by the Raleigh scattering equation and is directly proportional to the atmospheric $\frac{P(r)}{T(r)}$:

$$\beta_m(r) = C_{air}\frac{P(r)}{T(r)}$$

Where:

$C_{air} = 3.786\times10^{-6}$ K hPa$^{-1}m^{-1}$ at 532 nm (2.4)

$P(r) =$ Pressure

$T(r) =$ Temperature

A summary of the HSRL system specification is presented in Table 2-1 and Table 2-2.

Parameter	**Value**
Wavelength	532.112 nm
Frequency Stability	<50 MHz/hour
Spectral Width (FWHM)	<0.5 pm (SLM)
Pulse Duration	180 ns
Pulse Repetition Rate	4 KHz
Average Power	0.25 W
Beam Profile	Gaussian (TM_∞)
Beam Diameter after Expansion	4 cm
Beam Divergence after Expansion	<0.13 mrad
Polarization Type	Linear(>1:1000)
Polarization Switching Rate	2 KHz

Table 2-1, HSRL Transmitter Specifications

Parameter	Value
Telescope Type	Dall-Kirkham
Telescope Diameter	0.5 m
Telescope Effective Focal Length	5.08 m
field of view	160 μrad
Interference Filter Bandwidth	0.3 nm
Fabry-Perot Etalon Bandwidth (daytime)	8 pm
Cross-Polarization Rejection	10^{-3}
Iodine Transmission Channel	
Signal Detected	Molecular
Detector Type	PMT
I_2 Notch Filter Bandwidth (FWHM)	1.8 pm
Combined Channel	
Signal Detected	Aerosol + Molecular
Detector Type	PMT

Table 2-2, HSRL Receiver Specifications

2.4 Calibration of HSRL Data

The HSRL is able to discriminate between photons backscattered from molecules and aerosols because of the Doppler broadening of the molecular backscattered return. The HSRL uses a beam splitter to separate the received photons into two channels. The molecular channel uses an iodine filter to separate the aerosol and molecular return. The laser is tuned to a narrow absorption peak in the iodine spectrum. Photons backscattered into the receiver that have not been Doppler broadened are absorbed in the iodine cell. Doppler broadened photons with wavelengths shifted off the absorption peak are transmitted through the cell. Because the Iodine filter has a finite width and is not a perfect absorber, there is leakage of aerosol backscattered photons through the cell and the center part of the molecular return is absorbed by iodine. The second channel is the combined channel which receives the both the molecular and aerosol backscattered photons.

To account for these imperfections, a calibration scan of the iodine spectrum is preformed before the HSRL is operated. During the calibration, the laser is tuned across the absorption peak of the iodine filter and both the combined and molecular signals are recorded. The fraction of the actual molecular signal measured in the molecular channel (Cmm) is measured by convoluting both the molecular and combined channels with the Doppler broadened molecular spectrum which is computed from an atmospheric temperature profile.

$$Cmm(r) = \frac{\sum_{n=N_o}^{n=N_L} \frac{dS_m}{dt}(\lambda_n) M_{spect}(r, \lambda_n - \lambda_o) dt \Delta\lambda}{\sum_{n=N_o}^{n=N_L} \frac{dS_{a+m}}{dt}(\lambda_n) M_{spect}(r, \lambda_n - \lambda_o) dt \Delta\lambda} \tag{2.5}$$

Where:

$Cmm(r) =$ Fraction of the molecular signal in the molecular channel

$M_{spect}(r, \lambda_n - \lambda_o) =$ Calculated molecular spectrum

$\frac{dS_m}{dt}(\lambda_n) =$ Calibration signal measured in molecular channel as function of $\lambda, \left(\frac{\text{photons}}{\text{second}}\right)$

$\frac{dS_{a+m}}{dt}(\lambda_n) =$ Calibration signal measured in combined channel as function of $\lambda, \left(\frac{\text{photons}}{\text{second}}\right)$

dt = Time of 1 range bin = 100ns

$\lambda =$ Wavelength

λ_o = Wavelength at center of iodine absorption peak

$N_o =$ Start of spectral scan

$N_L =$ End of spectral scan

$\Delta\lambda$ = Wavelength change between $n_2 - n_1$

The rejection efficiency of the iodine cell to aerosol backscattered photons is measured by tuning the laser to the absorption peak of the iodine cell and measuring the number of photons received in the molecular channel relative to the combined channel.

$$Cam = \frac{\frac{dS_m}{dt}(\lambda_o) dt}{\frac{dS_{a+m}}{dt}(\lambda_o) dt} \tag{2.6}$$

This gives the fraction of the aerosol signal in the molecular channel.

Using the calibration coefficients Cmm and Cam, the separated molecular and aerosol returns are computed.

$$\frac{dN_m}{dt}(r) = \frac{\frac{dS_m}{dt}(r) - Cam\frac{dS_{a+m}}{dt}(r)}{\eta(C_{mm}(r) - C_{am})}dt \tag{2.7}$$

$$\frac{dN_a}{dt}(r) = \frac{\frac{dS_{a+m}}{dt}(r) - \eta\frac{dN_m}{dt}(r)}{\eta} \tag{2.8}$$

Where:

$\frac{dN_m}{dt}r^2(r) =$ Number of molecular photons backscattered on to the receiver within the field of view.

$\frac{dN_a}{dt}r^2(r) =$ Range corrected aerosol signal backscattered on to the receiver within the field of view.

$\frac{dS_m}{dt}r^2(r) =$ Range corrected signal measured in the molecular channel

$\frac{dS_{a+m}}{dt}r^2(r) =$ Range corrected signal measured in combined channel

η = System efficiency factor of the combined channel

2.5 HSRL Atmospheric Measurements

With this information the optical depth between ranges r_o and r can be independently measured using the molecular return N_m (r) and β_m (r) computed from an independently supplied temperature profile.

$$\tau(r) - \tau(r_o) = \frac{1}{2}\ln\left(\frac{\beta_m(r)r_o^{\,2}}{\beta_m(r_o)r^2}\frac{N_m(r_o)}{N_m(r)}\right) \tag{2.9}$$

$$N_m(r) = \frac{dN_m}{dt} dt$$

$$N_a(r) = \frac{dN_a}{dt} dt$$

The average extinction cross-section between r_o and r is computed by taking the derivative of the optical depth:

$$\langle B_e(r, r_o) \rangle \left\langle \frac{\partial \tau}{\partial r} \right\rangle = \frac{\tau(r) - \tau(r_o)}{r - r_o} \tag{2.10}$$

The aerosol backscatter cross-section is computed using both channels and is given by:

$$\beta_a(r) \frac{P_a(\pi, r)}{4\pi} = SR(r) \beta_m(r) \frac{3}{8\pi} \tag{2.11}$$

Where the scattering ratio, $SR(r)$ is:

$$SR(r) = \frac{N_a(r)}{N_m(r)} \tag{2.12}$$

2.6 HSRL Measured Depolarization

The HSRL is also capable of measuring the depolarization of the backscattered photons. The polarization of the transmitted beam is rotated from perpendicular to parallel polarization using a Pockals cell and is rotated every other laser shot. A polarization filter is used in the receiver, so that only one polarization is transmitted through the receiver. With this arrangement, photons transmitted with the polarization perpendicular to the polarizing beam splitter will be transmitted through the receiver only if there polarization has been rotated by a scattering event. The ratio between the received signal from the alternating perpendicular and parallel laser shots gives the fractional depolarization ratio.

$$\text{Depolorization}=\frac{P_{\perp}(r)}{P_{\parallel}(r)} \tag{2.13}$$

2.7 The Backscatter Phase Function Measurement

Figure 2-1 presents an example of an HSRL inverted profile and measurements of aerosol backscatter cross-section, extinction cross-section, and backscatter phase function derived from the inverted data as discussed in section 2.3. The data presented in the figure is temporally averaged for three minutes and has been vertically filtered using a running mean of eleven bins corresponding to 165 meter resolution. A bin represents the maximum vertical resolution of the HSRL which is 15 meters. The optical depth is calculated from the difference between the measured molecular signal and the calculated molecular signal with no extinction as described in equation 2.5. Before the extinction cross-section is computed the inverted molecular signal is smoothed using a double pass filter. This filter uses the eleven bin averaged data and computes a second eleven bin running mean on the data.

With the independently measured aerosol extinction and backscatter cross-section and assuming no absorption, the backscatter phase function can be computed for each layer, $r_2 - r_1$ and is given by:

$$\frac{\mathrm{P}(\pi, r_2, r_1)}{4\pi} = \left\langle \frac{\beta_a(r_2, r_1)}{\beta_s(r_2, r_1)} \right\rangle \tag{2.14}$$

The backscatter phase function is presented in the right profile in Figure 2-1.

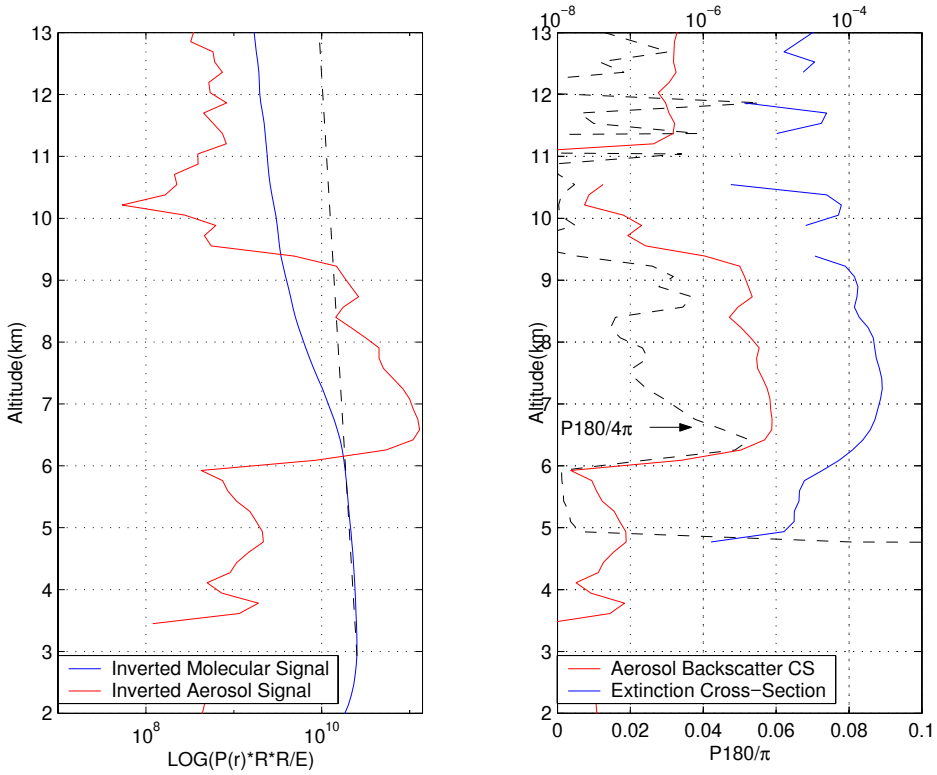

Figure 2-1, An HSRL inverted molecular and aerosol profile is presented in the left plot. The dashed line represents the molecular signal if there was no extinction. The aerosol backscatter cross-section, extinction cross-section, and backscatter phase function computed from the inverted profile is presented in the right profile. The axis for the backscatter phase function (P180/4π) is at the bottom of the figure. The units for the aerosol backscatter cross-section are (1/(m*sr). The data was taken on 22-Feb 2001.

C h a p t e r 3

3 HSRL Measurements

3.1 Introduction

There are two important innovations in this study. We present for the first time a large data set obtained with the HSRL that directly measures the backscatter phase function. Secondly, a rigorous error analysis was performed to quantify the reliability of the data which will be discussed in chapter 5. These advances have allowed important, new insights about the optical properties of cirrus clouds.

3.2 Measurement Collection Technique

To produce an unbiased data set, the HSRL was operated over an extended period including almost every day during 1994 when cirrus clouds where visible from the ground or satellite (74 days) and two times during 2001. I would like to thank Päivi Piironen for collecting the data for 1994.

Observations were made most frequently in the spring and fall due to the higher frequencies of cirrus cloud-producing synoptic disturbances (Figure 3-1). Because of the inability of the HSRL to penetrate clouds with optical depths greater then three, only cirrus clouds in the absence of optically dense low-level water clouds were investigated. Water clouds were removed from the data set by eliminating points with depolarization of less than 25%.

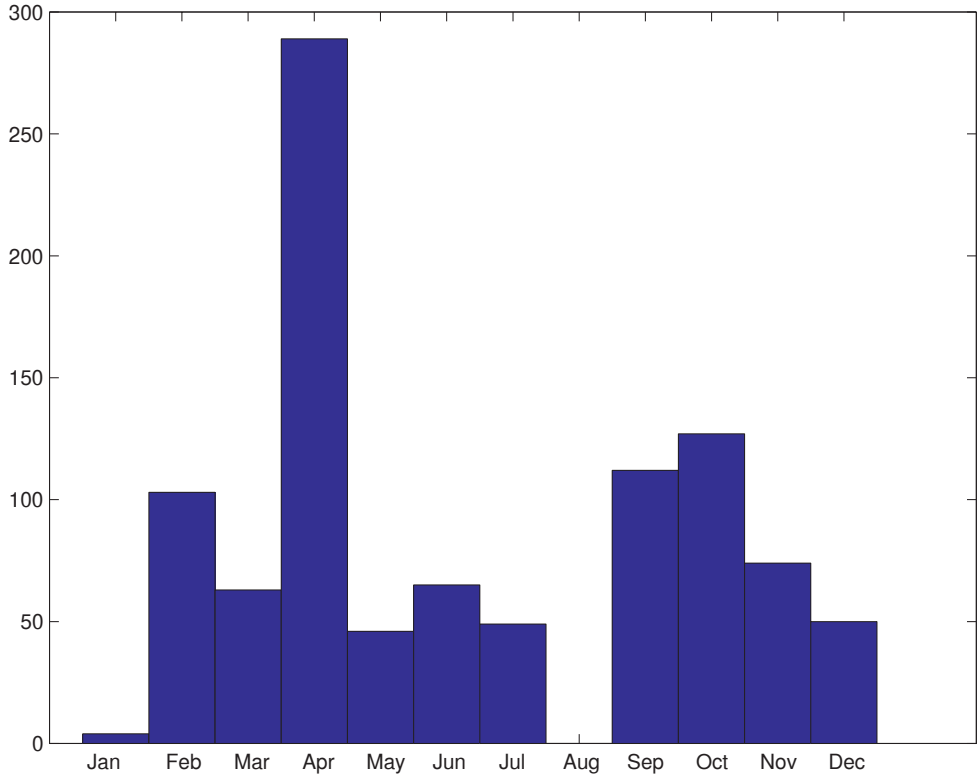

Figure 3-1, Number of data points for each month of the year that are included in the data set. Notice peak in the spring and fall (Months 4 and 9-10).

3.2.1 Photon Counting Errors

For photon counting instruments the random uncertainty is characterized by a Poisson distribution with one standard deviation equal to:

$$\sigma = \sqrt{N} \qquad (3.1)$$
$$N = \text{ Number of photons}$$

The HSRL has a vertical resolution of fifteen meters and temporal resolution of about three seconds. At this resolution the photon counting errors are large due to the

small number of photon collected. To decrease the errors associated with photon counting the data is averaged for approximately three minutes and vertically averaged over 165 meters. A detailed discussion of the calculation and magnitude of photon counting errors will be discussed in chapter 5.3.

3.2.2 Multiple Scatter Errors

The single scatter lidar equation assumes that when a photon is scattered it is removed from the beam. In reality, half the total scattered energy is scattered in the forward diffraction peak, some of which remains in the receiver field of view and contributes to the lidar signal. The magnitude of the multiple scattering effects is dependent on the extinction profile, scattering particle diameter, and the field of view of receiver. The particle size defines the angular width θ of the forward diffraction peak:

$$\theta \approx \frac{\lambda}{d} \tag{3.2}$$

where λ is the wavelength of the transmitted photons and d is the diameter of the scattering particles. For large particle diameters, θ is small resulting in the forward scattered energy remaining in the receiver field of view. Small particles result in a wider diffraction peak, with the forward scattered energy quickly leaving the receiver field of view. Figure 3-2 presents these two cases.

In the extreme case of very large particle diameters, all the forward scattered energy will remain in the field of view of the receiver through the cloud. The result is that the measured extinction in the cloud is half the actual value. A graphical depiction for this

case is presented in the bottom of Figure 3-2. Notice that the entire forward diffraction peak remains in the receiver field of view through the cloud. With this added energy, the molecular signal (red profile) is larger then the molecular signal without the forward diffraction peak (black profile). In this case the measured extinction would be half the actual value. For smaller particle diameters, the diffraction peak width is larger then the receiver field of view. The top of Figure 3-2 demonstrates the effect of the forward scatted energy on the received signal for this case. Near the base of the cloud the forward scattered energy decreases the slope of the molecular signal. This results in the underestimation of the extinction. This region is shaded orange in Figure 3-2. In the middle of the cloud (blue shading) assuming uniform extinction, the additional multiple scattered photons are balanced by the forward scattered photons exiting the receiver field of view. The slope of the molecular return (red profile) in the middle of the cloud in the top of Figure 3-2 is less affected by the forward scattering. Near the top of the cloud, the additional forward scattered energy contributes to the molecular signal, and the extinction is over estimated.

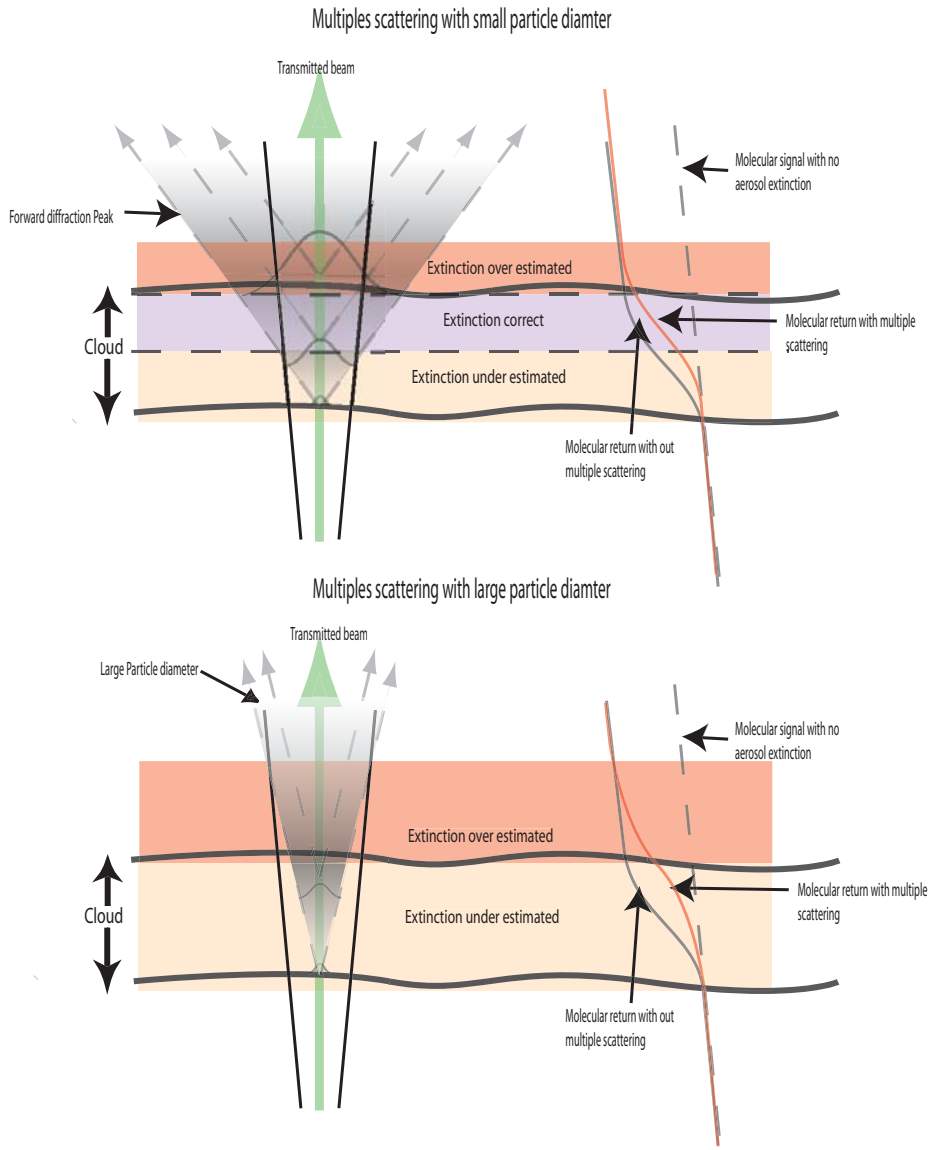

Figure 3-2, The effect of multiple scattering on HSRL measurements for a cloud with small and large diameter particles. The dashed arrows represent the width of the forward diffraction peak. The color shaded regions depicts the impact on the extinction caused by the forward scattered energy. The right side of the figure shows the molecular return with no multiple scatter effect (black profile) and with the multiple scatter contribution (red profile).

To minimize multiple scatter errors, the HSRL has a narrow 160 μrad receiver field of view that limits forward scattered energy in the receiver field of view. In addition, the data set is filtered to remove data where there are inhomogeneities in the aerosol backscatter cross-section. This was accomplished by eliminating data points when the measured aerosol backscatter cross-section differed by more then 30% when compared to adjacent points in the vertical. The effectiveness of the filter will be discussed in chapter 5.6.

3.3 Statistical Distribution of Backscatter Phase Function

The distributions of the backscatter phase function determined with the HSRL with different error thresholds are shown in Figure 3-3. The backscatter phase function values in cirrus clouds have a broad distribution with a dominant peak. The measured values of the backscatter phase function range from 0.02 to 0.14, consistent with the contribution of many different ice crystal types to the optical properties of cirrus clouds. The general shape of the distributions is independent of the error threshold.

The distribution of backscatter phase function measurements are compared to modeled calculations of backscatter phase functions for select pristine crystal types (Yang) and (Macke, 1998). The modeled phase functions are presented on top of Figure 3-3. Notice that the peak of the distribution, centered at 0.04 is consistent with bullet rosettes, spheres and solid columns.

A striking result of the study was the finding that the probability distribution of backscatter phase function has a dominant peak at approximately 0.04 in Figure 3-3.

Because this peak was observed even at the most stringent error threshold, it is likely to represent an important optical characteristic of cirrus clouds. However, the distribution width suggests that a wide range of backscatter phase function values are possible. The results are consistent with a similar but broader peak in the distribution of the backscatter phase function values obtained by (Sassen, 2001) using a different technique.

Regular crystal types that have been identified in cirrus clouds have different backscatter phase functions calculated by ray tracing techniques in Figure 3-3. There are several crystal forms that have calculated backscatter phase functions of approximately 0.04 which could account for the observed maximum in the distribution. However, if these forms were responsible, the depolarization associated with the peak should have a non-random distribution. This was not the case as seen in Figure 3-5. It is more likely that the peak in the backscatter phase function results from irregular crystals. Even slight perturbations from a regular structure can have large effects on the mean scattering properties (Macke, 1998). Experiments using particle replicators (Heymsfield, 1990) have shown wide variations in cirrus ice crystal structure, many which are not regular. Laboratory experiments demonstrate that sublimation from initially prismatic crystals causes rounding of crystal edges, (Nelson, 1998) which will have profound effects on the backscatter phase function. Crystals with rounded corners will not be efficient corner-reflectors and will have significantly smaller backscatter phase functions when compared to a pristine crystal.

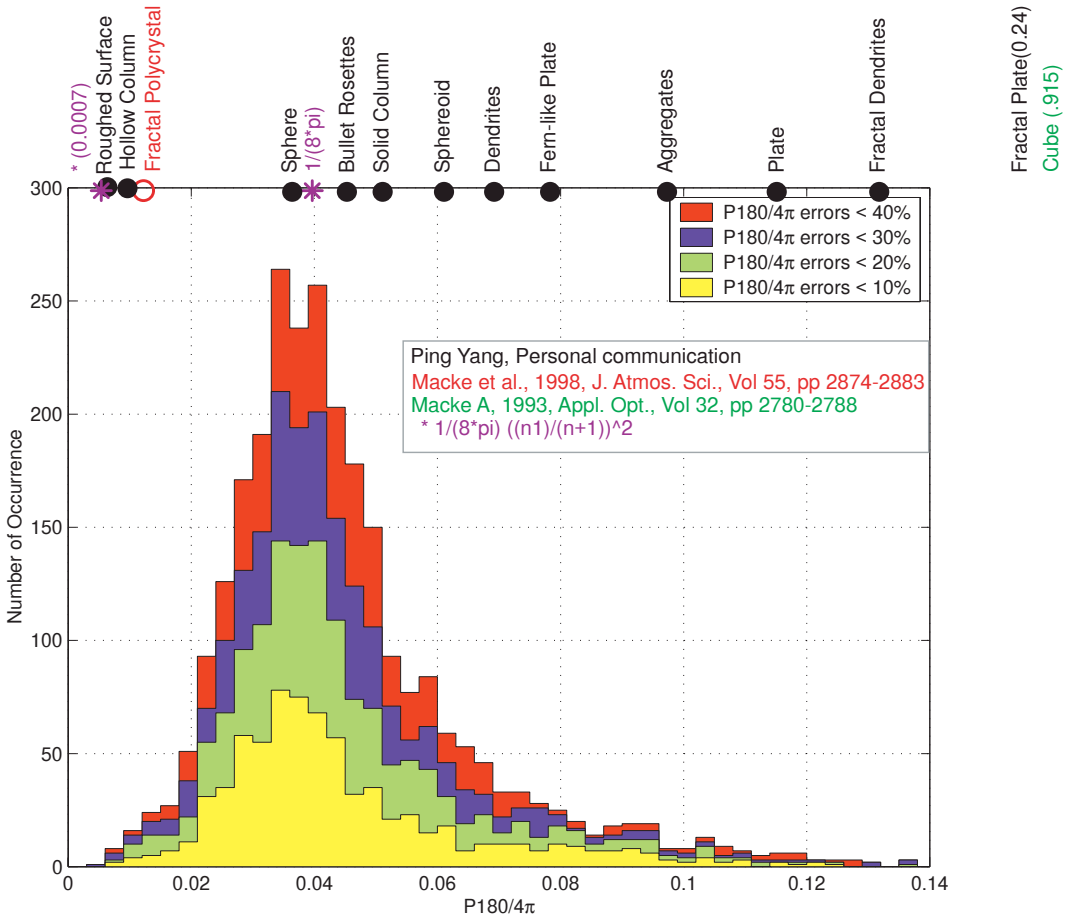

Figure 3-3, Point by point distributions of backscatter phase functions measurements made during 1994 and 2001. There are four distributions plotted, each representing different statistical error threshold criteria. Calculated ray tracing backscatter phase functions for different crystal types are plotted at the top of the figure (Yang), (Macke, 1998).

3.4 Short Term Distributions of the Backscatter Phase Function

Figure 3-3 summarizes all the data accumulated over 76 sessions. The data could reflect the distributions of different backscatter phase functions from different sessions or could reflect a common characteristic of the majority of ice clouds. Because of improvements

in the HSRL, we have recently been successful in obtaining sufficient data from single sessions to determine single session distributions. Figure 3-4 presents a histogram of the backscatter phase function measurements for February 20 and February 22, 2001. The distributions from both days had prominent peaks between 0.03 and 0.04. Thus, one of the prominent aspects of the ensemble of distributions, the peak at 0.04 Figure 3-3, reflects the characteristics for these days. However, Figure 3-3 suggests that their can be large variability in the back scatter phase function for individual days.

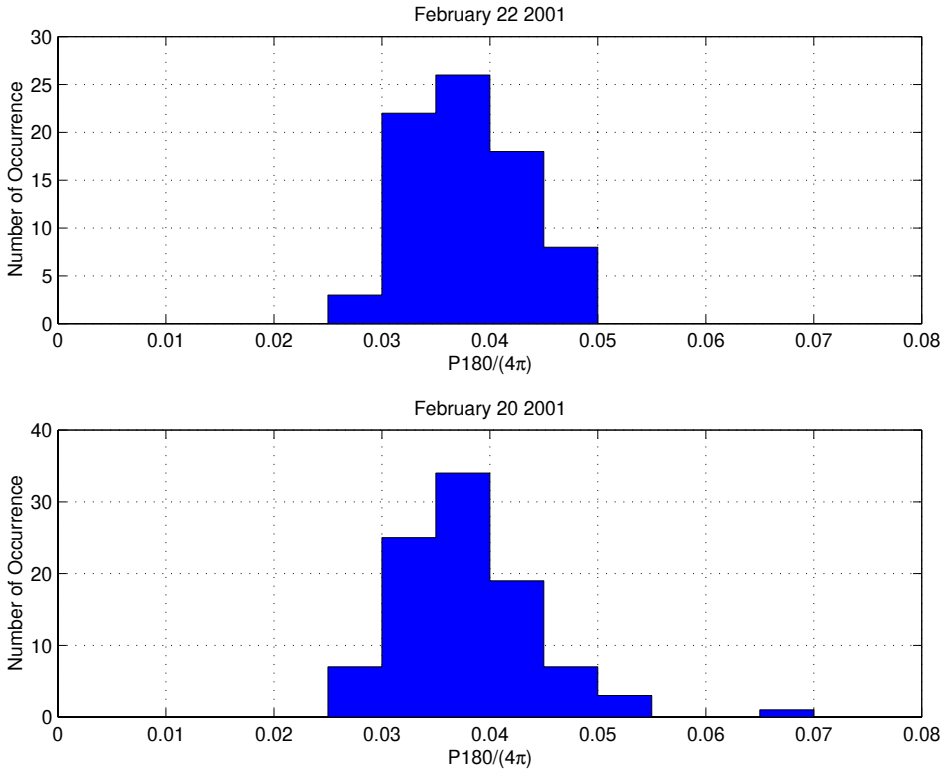

Figure 3-4, Short term distributions of the backscatter phase function for February 20 and February 22, 2001. The same filter criteria as Figure 3-3 has been applied. The data was filtered using with a photon counting error threshold of < 40 %.

3.5 Depolarization Dependence of the Backscatter Phase Function

Figure 3-5 presents the phase-function as a function of depolarization. The data is filtered using the same filtering criteria used in Figure 3-3 except only measurements with the backscatter phase function errors less then 20% are included. Each data point has a computed statistical error represented by a one standard deviation error bar. The mean value of the backscatter phase function was computed for depolarization intervals of 0.05, represented by the blue line in the figure. Notice the positive correlation between the backscatter phase functions at large depolarizations.

The peak in the backscatter phase function distribution of 0.04 in Figure 3-3 is associated with a wide range of depolarizations in Figure 3-5. There appears to be a correlation between points with very large backscatter phase function values and high depolarizations. Figure 3-5 shows that the peak of the backscatter phase function between 0.02 – 0.08 is correlated with depolarization values between 0.25 – 0.45. Backscatter phase function values greater then 0.1 are associated with depolarizations between 0.45 - 0.56.

There is a small group of measurements that have depolarization greater then 0.50 but a relatively small backscatter phase function compared to measurements with large depolarization as seen in Figure 3-5. The measurements are from one data session that had a high thin ice cloud with atmospheric temperatures colder then -55 o C. This could represent a case with pristine crystals.

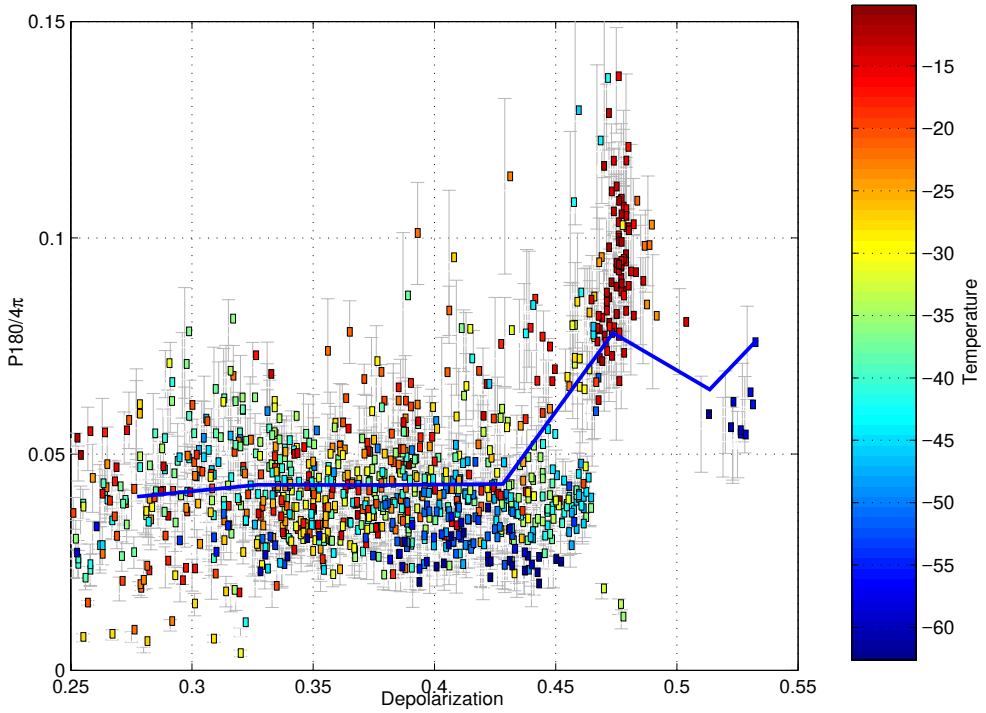

Figure 3-5, The backscatter phase function with respect to depolarization for the point-by-point measurements. Only points with backscatter phase function errors less then 20%, depolarization > 25%, and the non-uniformity criteria < 30% are included. The color of each data point is representative of the measured temperature at the level that the data was taken. The error bars represent one standard deviation statistical error. The color representing the temperatures can be seen in the color bar associated with the figure. The blue line represents the mean backscatter phase function value calculated at 0.05 depolarization increments.

The data suggests that there is a distinct difference between crystals associated with the peak of the backscatter phase function and the larger values in the wings of the distribution. This supports the theory that the peak of the backscatter phase function distribution in Figure 3-3 is composed of irregular crystals while the larger values represent cases with regular crystals types. Pristine crystals that have internal corners make very efficient corner reflectors. Light entering the crystal has to pass through tilted

surfaces, inducing depolarization. In contrast, irregular crystals with rounded internal corners and irregular surfaces will not be efficient corner reflectors. For these crystals, in order for energy to be backscattered, a larger fraction of the backscattered photons will come from the facets that are oriented perpendicular to the lidar beam. These reflections have little effect on the polarization and are not efficient reflectors because the Fresnel reflectivity of ice is low. The result is that irregular crystals will have smaller backscatter phase functions and depolarization while pristine crystals will have larger backscatter phase functions and depolarization. It is important to note that the above discussion is a possible explanation for the observed backscatter phase function peak and the correlation with depolarization. In future work it would be interesting to compare ray tracing calculations of the backscatter phase function for irregular crystal types with the HSRL measurements.

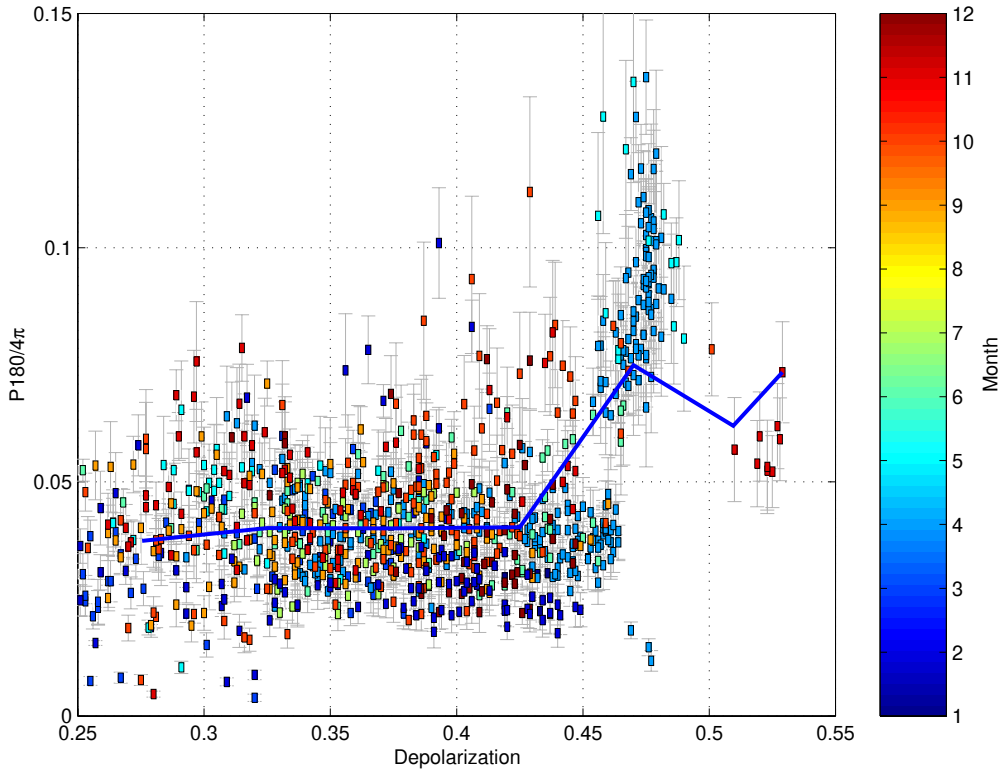

Figure 3-6, The backscatter phase function with respect to depolarization for the point-by-point measurements. Only points with backscatter phase function errors less then 20%, depolarization > 25%, and the non-uniformity criteria < 30% are included. The color of each data point is representative of the day the data was collected. The error bars represent one standard deviation statistical error. The color representing the day the data was collected can be seen in the color bar associated with the figure. The blue line represents the mean backscatter phase function value calculated at 0.05 depolarization increments. It is important to note that the group of data points with large depolarizations and backscatter phase functions are from more then one day.

3.6 Temperature Dependence of Backscatter Phase Function

A dependence of the backscatter phase function on temperature has been suggested. It has been shown that crystal type is strongly dependent on temperature. Ray tracing calculations show large differences in the backscatter phase function for different crystal

types. The range of the calculated backscatter phase function values for different crystal types can be seen on top of Figure 3-3. Because both temperature and the backscatter phase function are correlated with crystal type, a dependence of the backscatter phase function on temperature could be expected.

The HSRL measurements do show a dependence of the backscatter phase function with temperature as seen in Figure 3-7 and Figure 3-5. The figures suggests that it is more likely to have large backscatter phase functions at warmer temperatures.

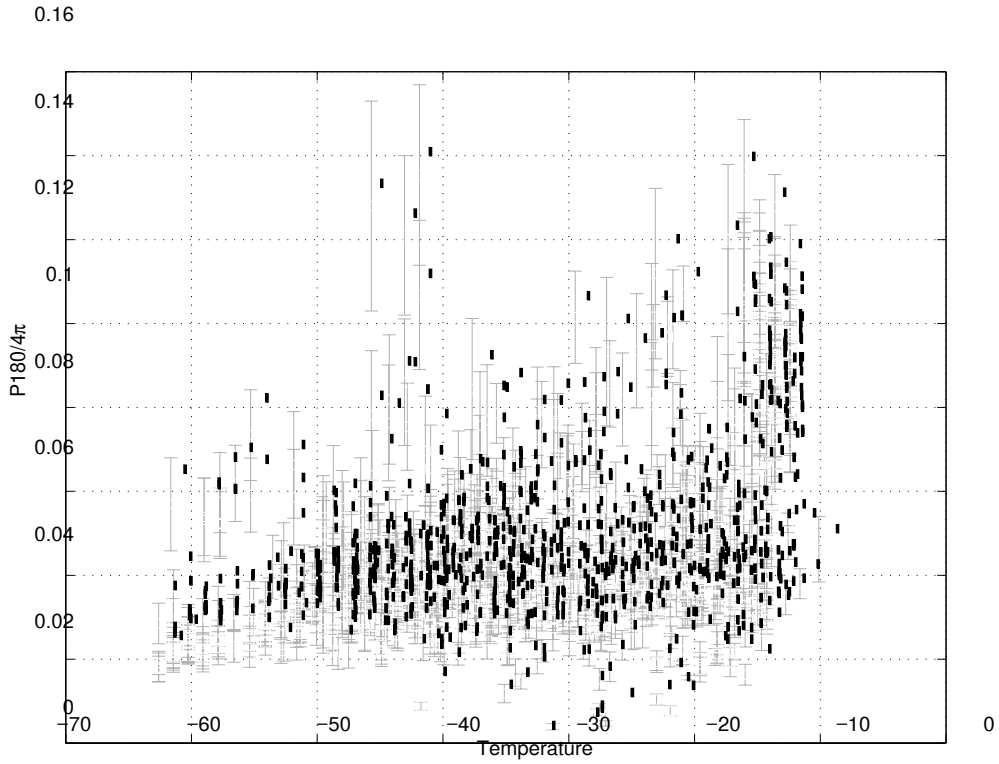

Figure 3-7, Backscatter phase function plotted with respect to temperature for the point-by-point measurements. The same filter criteria as Figure 3-3 except that only points with backscatter phase function errors of less then 20% are included. A one standard deviation photon counting error is represented by the error bars.

.

C h a p t e r 4

4 The Bulk Backscatter Phase Function

To further increase the confidence in the data set a bulk backscatter phase function was computed. Instead of computing the extinction from the derivative of the optical depth in the point-by-point method, the bulk backscatter phase function is computed using the optical depth of the entire cloud and the integrated backscatter cross-section. The bulk backscatter phase function is then:

$$\frac{\overline{P(\pi,r,r_o)}}{4\pi} = \frac{\int_{r_o}^{r} \beta_s(r)\frac{P(\pi,r)}{4\pi}dr'}{\int_{r_o}^{r} \beta_s(r)dr'} = \frac{\int_{r_o}^{r} \beta_a(r,r_o)\frac{P(\pi,r)}{4\pi}dr'}{\tau(r)-\tau(r_o)} \qquad (4.1)$$

Where r_o is located at the base of the cloud and the range r is located well above the cloud top. The advantage of the bulk backscatter phase function is that it is less sensitive to multiple scattering errors. The optical depth is measured well above the top of the cloud where most of the small angle, forward scattered photons have exited the receiver field of view. The high sensitivity to noise in the derivative of the optical depth is also decreased because the entire optical depth of the cloud is used. Figure 4-1 show the frequency of occurrence of the bulk backscatter phase function for 17 clouds. Only uniform clouds were selected to minimize the effect of averaging over inhomegineties. The bulk backscatter phase function distribution shows a peak at approximately 0.04 which correlates well with the point-by-point distribution in Figure 3-3. This strong correlation increases the confidence that the filtering criteria used in the point-by-point

distribution are effective in limiting the multiple scattering and noise on the results. The bulk backscatter phase function value at 0.08 in Figure 4-1 has been investigated and was found to be valid. It represents real variability in the backscatter phase function.

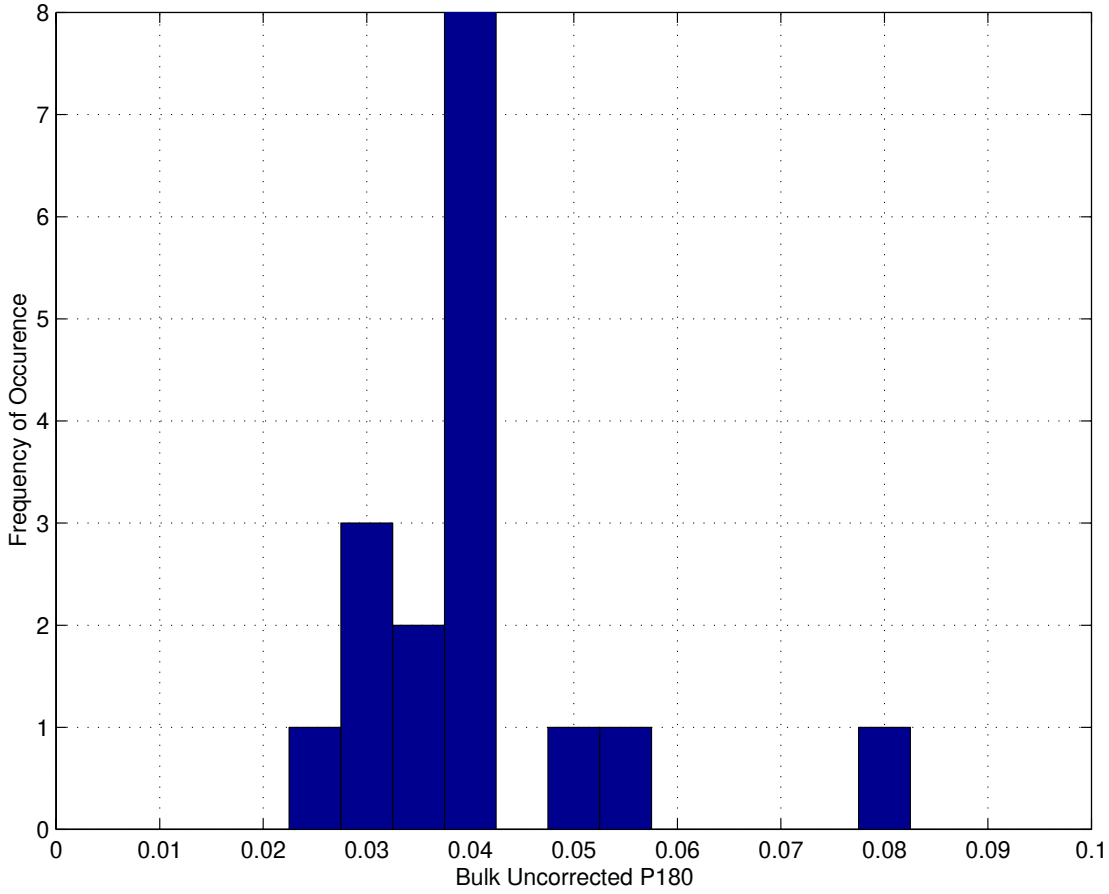

Figure 4-1, The bulk backscatter phase functions for hand-selected cases during 1994 and 1996. Notice the peak is similar to Figure 3-3.

Chapter 5

5 Error Analysis

5.1 Introduction

The significance of a measurement is dependent on the ability to determine its uncertainties. With a single channel lidar it is difficult to quantify the uncertainties in the extinction and backscatter cross-section because assumptions about the relationship between the extinction and backscatter cross-section are needed. Because the HSRL is capable of measuring the extinction and backscatter cross-section independently, the backscatter phase function and its uncertainties can be quantified.

The errors in the HSRL measurements can be separated into four categories:

1. Photon counting errors
2. Calibration errors
3. Multiple scattering errors
4. Errors caused by non linear averaging

In this section the methods used to measure or estimate these errors will be discussed.

5.2 HSRL Photon Counting Errors

The HSRL raw data consists of the combined and molecular signal, each having its own statistical error. For photon counting instruments, such as the HSRL the statistical uncertainties are characterized by a Poisson distribution with one standard deviation equal to:

$$\sigma = \sqrt{N} \qquad (5.1)$$

$N =$ Number of counts

The statistical errors in the raw data can be propagated through the lidar equation to give the photon counting errors in the HSRL measured optical properties.

The errors in the raw data are propagated through the lidar equation by taking the partial derivatives with respect to each of the raw measurements multiplied by the statistical error in the measurement. The error equation for the backscatter phase function is shown in equation 3.2.

$$\sigma^2_{\frac{P(\pi,r,r_o)}{4\pi}} = \sigma^2_{Mraw}\left(\frac{\partial \frac{P(\pi,r,r_o)}{4\pi}}{\partial Mraw}\right)^2 + \sigma^2_{Craw}\left(\frac{\partial \frac{P(\pi,r,r_o)}{4\pi}}{\partial Craw}\right)^2 +$$

$$\sigma^2_{\rho}\left(\frac{\partial \frac{P(\pi,r,r_o)}{4\pi}}{\partial \rho}\right)^2 + 2\times\left(\frac{\partial \frac{P(\pi,r,r_o)}{4\pi}}{\partial Mraw}\right)\left(\frac{\partial \frac{P(\pi,r,r_o)}{4\pi}}{\partial \rho}\right)\sigma^2_{(Mraw)(\rho)}\ldots$$

$\sigma_{\frac{P(\pi,r,r_o)}{4\pi}}$ = STD of the backscatter phase function

σ_{Mraw} = STD of the Molecular signal (5.2)

σ_{Craw} = STD of the combined signal

$\sigma\rho$ = STD of the estimated error in the density profile

$\sigma^2_{(Mraw)(\rho)}$ = Covariance between the density and molecular channel

The terms that account for correlations between the raw measurements appear at the end of the equation. For example, the correlation between the molecular channel and the density profile is represented by the term $2\times\left(\frac{\frac{P(\pi,r,r_o)}{4\pi}}{\partial Cmm}\right)\left(\frac{\frac{P(\pi,r,r_o)}{4\pi}}{\partial\rho}\right)\sigma^2(Craw)(\rho))$.

It is has been demonstrated that Cmm is insensitive to errors in the density profile (Piironen, 1994). For this reason this correlated component is not included in the error equation. To minimize the effect of correlated measurements the error equation for the optical depth and aerosol backscatter cross-section were propagated directly from the raw data. The complete error equations used for the analysis are in Appendix A.

The error in the density profile is assumed to be random. The density profiles used for the measurements are obtained from radiosonde profiles taken in Green Bay, Wisconsin located 150 km north of Madison. The primary error is caused by the geographic and temporal separation. The temporal errors result from the difference in time between the temperature profile and data collection time. This difference can be as large as six hours. To estimate the magnitude of the geographic error, profiles of the atmospheric mean lapse rate measured at Green Bay, Wisconsin were compared to Davenport Iowa located 400 km southwest of Green Bay. The mean difference in lapse rate between altitudes of 5 and 10 kilometers was found to be $0.67\frac{K}{km}$ with a standard deviation of $0.7\frac{K}{km}$ over a one year period. Because Madison is 150 km from Green Bay

this error should be smaller. The temporal error was calculated by comparing the change in lapse rate between 5 km and 10 km for a 12 hour separation at Green Bay, WI. The mean difference in the lapse rate for one year of sounding data was $1.2\frac{K}{km}$ for a 12 hour difference. Because radiosondes are launched every 12 hours, a maximum difference of 6 hours between data collection and radiosonde launch can occur. The lapse rate error should be smaller then the 12 hour difference. For this analysis a lapse rate error of $1.0\frac{K}{km}$ will be used.

For individual days, the error in the density profile may not be random due to the organized structure of the atmosphere. For a large number of measurement days the treatment of the atmospheric density as a random error becomes a better approximation assuming that there is not a consistent trend in the density profile between Madison and Green Bay.

The HSRL optical depth and extinction measurements are primarily sensitive to the errors in the lapse rate of the temperature profile, $\frac{\partial T}{\partial r}$. The absolute error in the temperature effects the error in the calibration coefficient Cmm but this error has been demonstrated to be small (Piironen, 1994). For the optical depth, the magnitude of the

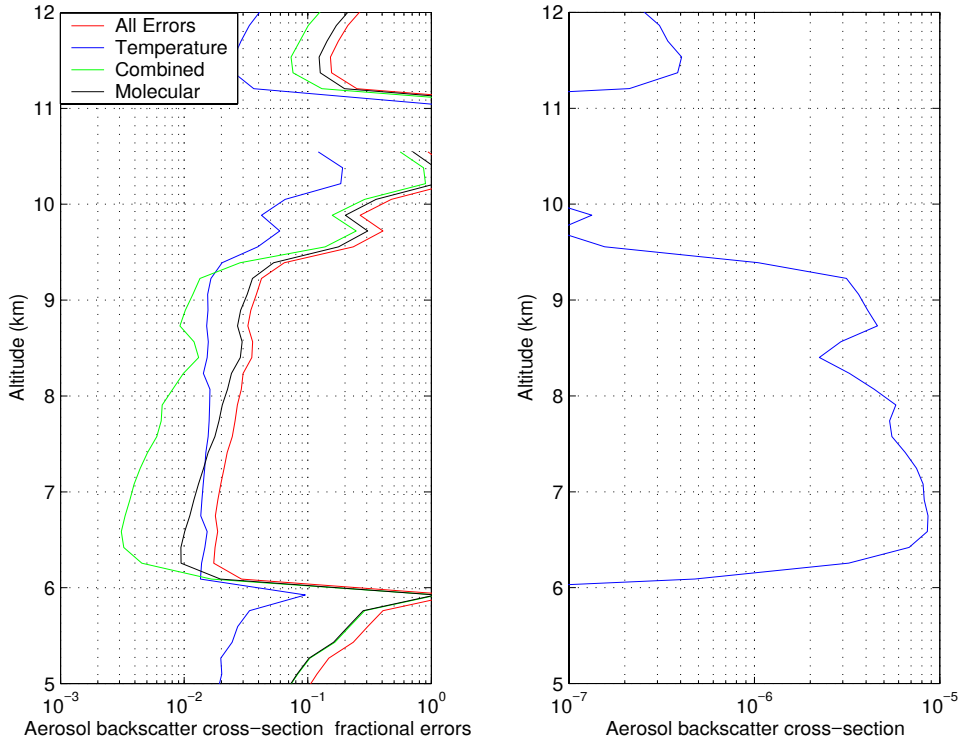

Figure 5-1, HSRL measured aerosol backscatter cross-section and the associated fractional errors. The profile was computed using a 3 minute average on February 22, 2001 corresponding to 02:43:48 - 02:46:56 UT. The effects of the individual errors on the measurement are color coded in the left panel.

error increases with range and is computed as a function of height $\sigma_{Temp} = \frac{\partial T}{\partial r} \times r$ normalized to zero at 5 km to correspond to the start of the optical depth profiles.

The HSRL error equation 3.3 has been implemented into the HSRL data processing software so that all statistical errors are calculated for the aerosol backscatter cross-section, optical depth, extinction cross-section and backscatter phase function as part of the routine data processing

5.3 The Effect of Photon Counting Errors on HSRL Measurements

The magnitude of the individual fractional errors for the profile of aerosol backscatter cross-section taken with 3-minute averages on February 22, 2001 is presented in Figure 5-1. The statistical error in backscatter cross-section is most sensitive to the uncertainties in the temperature profile near the cloud base. Above 7.5 km the error in the molecular signal is most significant.

Figure 5-2 presents the optical depth profile and fractional errors for the same period as Figure 5-1. The dominant error in the optical depth measurement is the uncertainties in the molecular channel. Notice the minimum error occurs at approximately 8 km with larger errors at the beginning and end of the cloud. The large fractional errors at the base of the cloud demonstrate the limitations of the sensitivity of the optical depth measurements. At the base of the cloud photon counting statistics are small but the optical depth is small. Small amounts of noise can result in large fractional fluctuations at small optical depths. At the top of the cloud, photon counting errors dominant the optical depth errors because of the attenuated signal and the $\frac{1}{r^2}$ dependence.

The extinction cross-section is computed by taking the difference between the optical depths at adjacent ranges.

$$\left\langle \beta_e(r, r_o) \right\rangle = \left\langle \frac{\partial \tau}{\partial r} \right\rangle = \frac{\tau(r) - \tau(r_o)}{r - r_o} \tag{5.3}$$

The optical depth τ is sensitive to noise in the molecular signal as seen in Figure 5-2. Because the difference in the optical depth between adjacent points is small, the

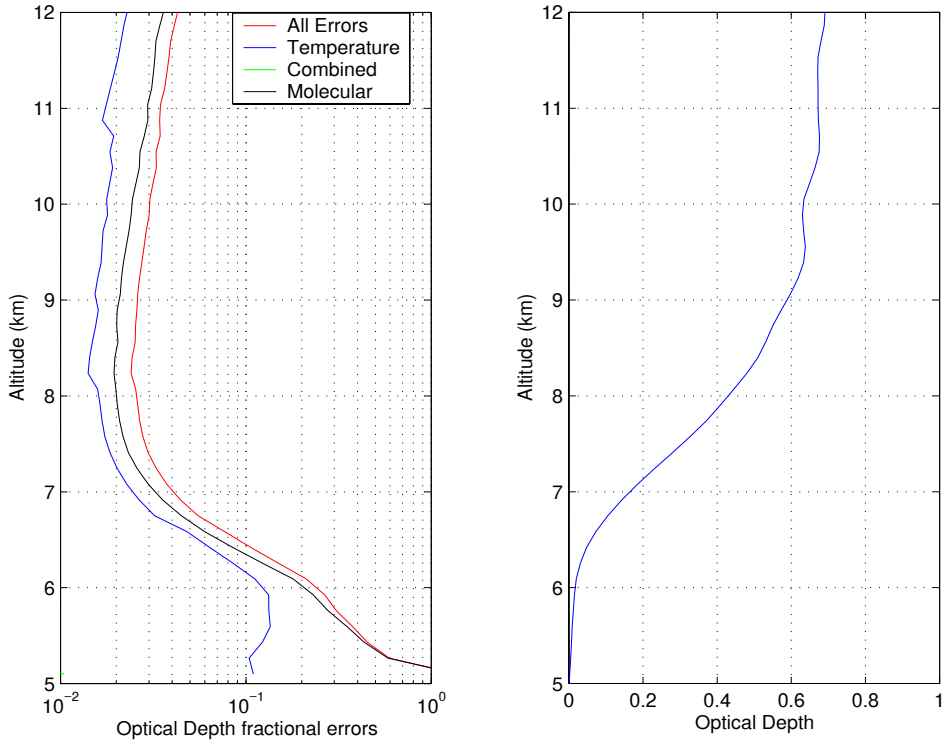

Figure 5-2, HSRL optical depth profile and associated fractional errors for February 22, 2001, 02:43:48 - 02:46:56 UT. The molecular signal has been vertically averaged using an 11 bin average resulting in 165 m resolution. The optical depth is normalized to zero at 5 km.

extinction is extremely sensitive to this noise. To improve the reliability of the extinction measurement the molecular signal is smoothed using a double pass filter as discussed in Chapter 2.7. The errors presented in Figure 5-2 include this filter. The extinction for February 22, 2001, 02:43:48 - 02:46:56 UT and associated errors are presented in Figure 5-3. Notice that the errors in the extinction are dependent on the uncertainties in the molecular signal and temperature. The uncertainties in temperature lapse rates are also important. The combined signal has little effect on the measurement

because the extinction is calculated from the differences in the molecular signal. The only contribution to the extinction from the combined channel is from the subtraction of aerosol photons from the molecular channel as discussed in section 2.4.

The backscatter phase function is dependent on both the errors in the aerosol backscatter cross-section and extinction cross-section.

$$\left\langle \frac{P(\pi, r, r_o)}{4\pi} \right\rangle = \left\langle \frac{\beta_a(r, r_o)}{\beta_s(r, r_o)} \right\rangle \tag{5.4}$$

Figure 5-4 presents a profile of the backscatter phase function and its associate errors. The uncertainties in the extinction dominate the error in the backscatter phase function. The error in the aerosol backscatter cross-section has only a 1.0% -2.0 % effect on the backscatter phase function measurement.

The total error in the backscatter phase function is large compared to the errors in the backscatter cross-section and optical depth. In this profile, the fractional errors range from 15% – 100% in the cloud.

The backscatter phase function profile in the right plot has a large peak at the base of the cloud. This observed peak is most likely due to the multiple scatter contribution. As discussed in chapter 3.2.2 the contribution to the signal due to multiple scattering results in an underestimation of the extinction at the base of the cloud. The result is that the backscatter phase function is measured too large. Because half the energy is contained in

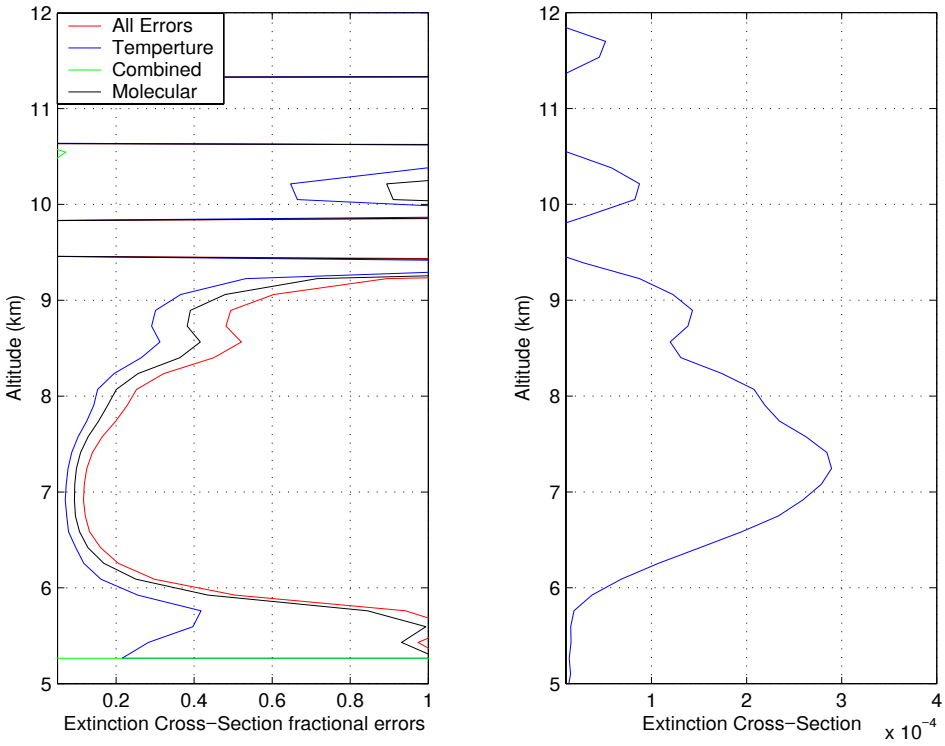

Figure 5-3, The HSRL Extinction cross-section profile and its associated fractional errors for the February 22, 2001, 02:43:48 - 02:46:56 UT.

the forward diffraction peak, the error can result in a factor two difference in the backscatter phase function.

5.4 Non Linear Averaging Errors

The statistical errors can be reduced by averaging the data. The longer the data is averaged, the smaller the statistical errors. Averaging comes at a cost, the temporal resolution is reduced and errors caused by averaging the non linear returned signal over cloud inhomogeneities are introduced. The measurements presented in chapter 3 are averaged for three minutes. The averaging time was used to reduce the statistical errors

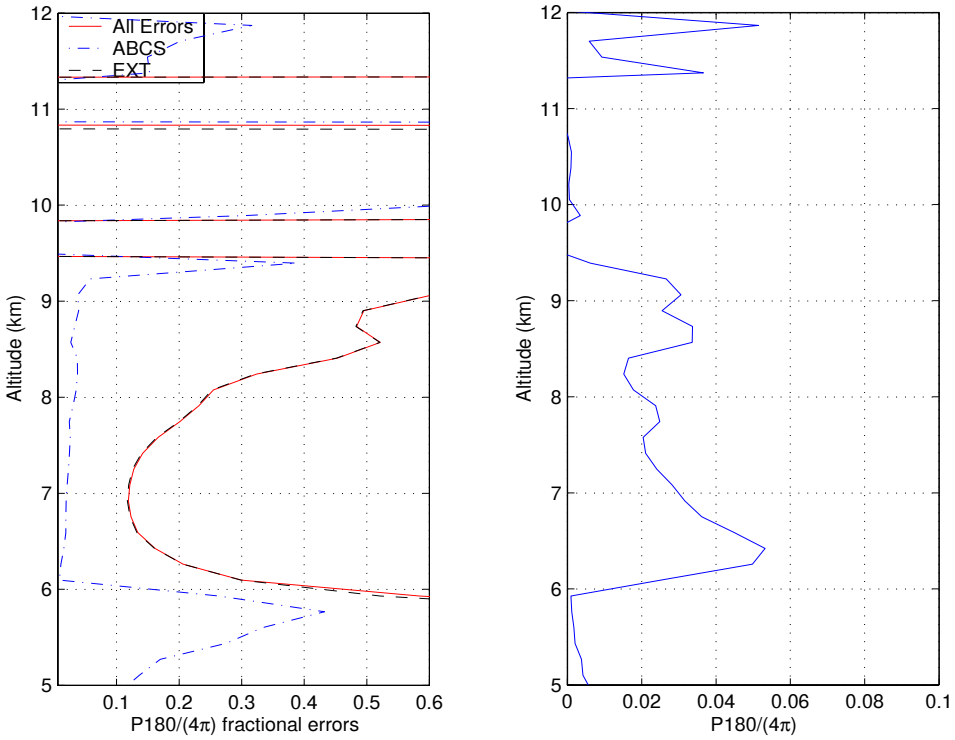

Figure 5-4, The HSRL Backscatter phase function profile and the associated fractional errors for February 22, 2001, 02:43:48 - 02:46:56 UT. The effects of the aerosol backscatter cross-section, extinction, and combined errors are presented in the left panel in the left panel.

but not introduce large non-uniformity errors. Assuming a cloud is moving over the lidar at 25 m/s, a three-minute average will result in a 4.5 km cross-section of the cloud.

5.5 Calibration Errors

As discussed in chapter 2.4, calibration coefficients are computed to account for the "cross-talk" between the combined and molecular channel. The leakage of aerosol backscattered photons through the iodine cell and the fraction of the molecular backscattered photons that are not transmitted through the molecular channel must be accounted for by the calibration coefficients Cam and Cmm. Uncertainties in these

coefficients effect the accuracy of the atmospheric measurements. The calibration errors can be divided into 4 categories:

1. Optical misalignments in the system

2. laser spectral tuning errors

3. Uncertainties in the atmospheric temperature profile.

4. Photon counting errors associated with measuring the calibration coefficients.

The errors caused by misalignments in the system and uncertainties in the temperature profile are not random and must be treated separately from the random error analysis.

Before each data session a calibration scan is preformed. Light from the transmitted laser pulse is injected into the receiver. To correctly measure Cam and Cmm, the injected light must replicate the atmospheric return. This requires illuminating the receiver identically compared to the atmosphere.

To investigate the sensitivity of the calibration coefficients on the backscatter phase function measurements, the coefficients are shifted and the change in the backscatter phase function is computed using the shifted coefficients. They are then compared to the backscatter phase function computed using the unmodified calibration coefficients. This method is applied to an optically thin profile (optical depth < .2) and an optically thick profile (optical depth > 1.5) to investigate the sensitivity of calibration errors to varying optical thicknesses.

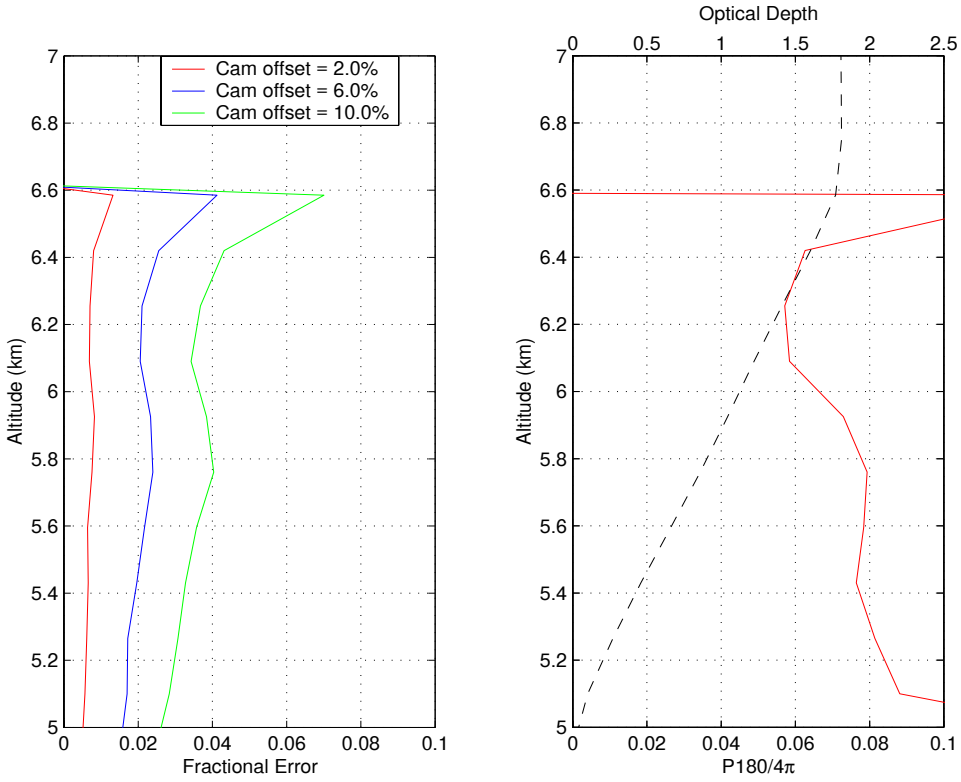

Figure 5-5, Figure The HSRL measured backscatter phase function and optical depth profile is presented in the right plot for Apr 26, 1994. The axis representing the optical depth and backscatter phase function is located at the top and bottom of the figure. The fractional change in the backscatter scatter phase function due to varying Cam is presented as a function of range in the left profile.

It has been demonstrated by (Piironen, 1994) that the uncertainty in Cam is ≈ 2.0%. This corresponds to an error of approximately 1.0% in the backscatter phase function measurement. The effect of the systematic errors on the calibration coefficient Cam for a cloud with an optical thickness of 1.7 is presented in Figure 5-7. Excluding cloud edges, the errors in the backscatter phase function due to Cam range from 1.0% to 7.0%. This is dependent on the magnitude of the offset of Cam and the location in the cloud.

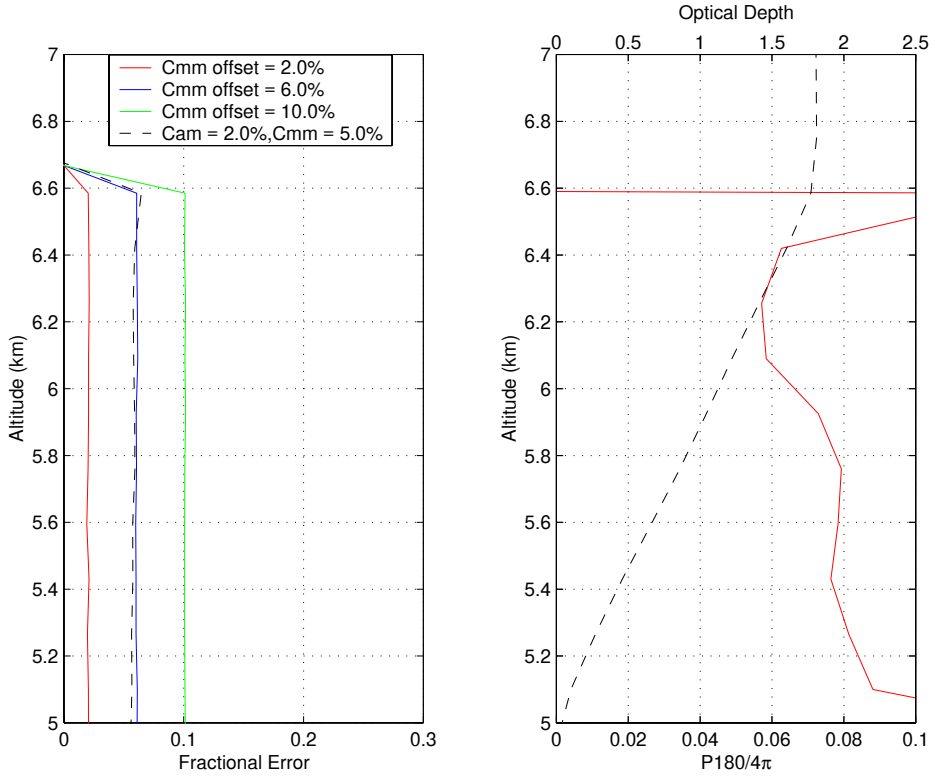

Figure 5-6, The HSRL measured backscatter phase function and optical depth profile is presented in the right plot for Apr-26, 1994. The axis representing the optical depth and backscatter phase function is located at the top and bottom of the figure. The fractional change in the backscatter scatter phase function due to varying the calibration coefficient Cmm is presented as a function of range in the left profile. The dashed error profile is the fractional change in the backscatter phase function with a 2% offset in Cam and a 5% offset in Cmm.

The errors associated with the calibration coefficient Cmm for the same profile as Figure 5-5 is presented in Figure 5-6. A 2% offset in Cmm results in a 2-3% error in the backscatter phase function. An error of 10% in Cmm changes the backscatter phase function by 10%. The uncertainty in Cmm is estimated to be ≈ 5.0% (Piironen, 1994). The error will result in a 5.0% error in the backscatter phase function measurement. The dashed profile in Figure 5-6 is the error in the backscatter phase function resulting from

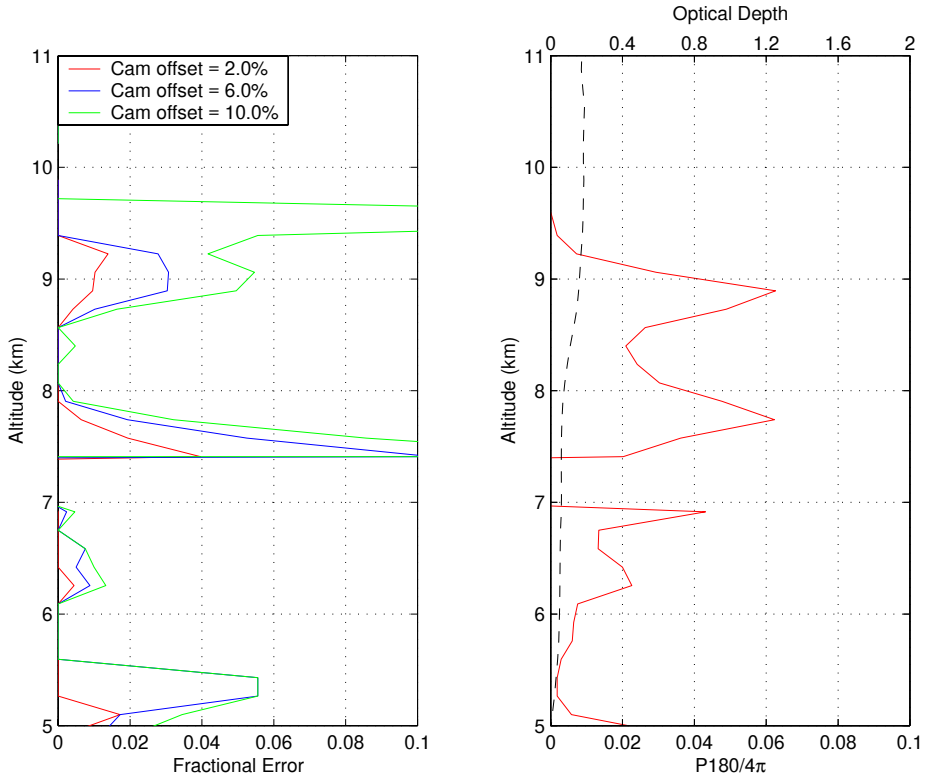

Figure 5-7, The HSRL measured backscatter phase function and optical depth profile is presented in the right plot for Feb-22 2001. Notice the total optical depth of only 2.0. The axis representing the optical depth and backscatter phase function is located at the top and bottom of the figure. The fractional change in the backscatter scatter phase function due varying differences in the offset of the calibration coefficient Cam is presented as a function of range in the left profile.

an offset in Cam and Cmm of 2.0% and 5.0% respectively. The combined error is approximately 5.0%.

Figure 5-7 and Figure 5-8 use the same technique but are applied to the thin cloud. The sensitivity of the backscatter phase function measurement to errors in Cmm is slightly larger for the optically thin cloud. A 10.0% error in Cmm results in 12% error for the optically thin cloud (Figure 5-8) in contrast to the optically thick cloud which has an error of 10% (Figure 5-6).

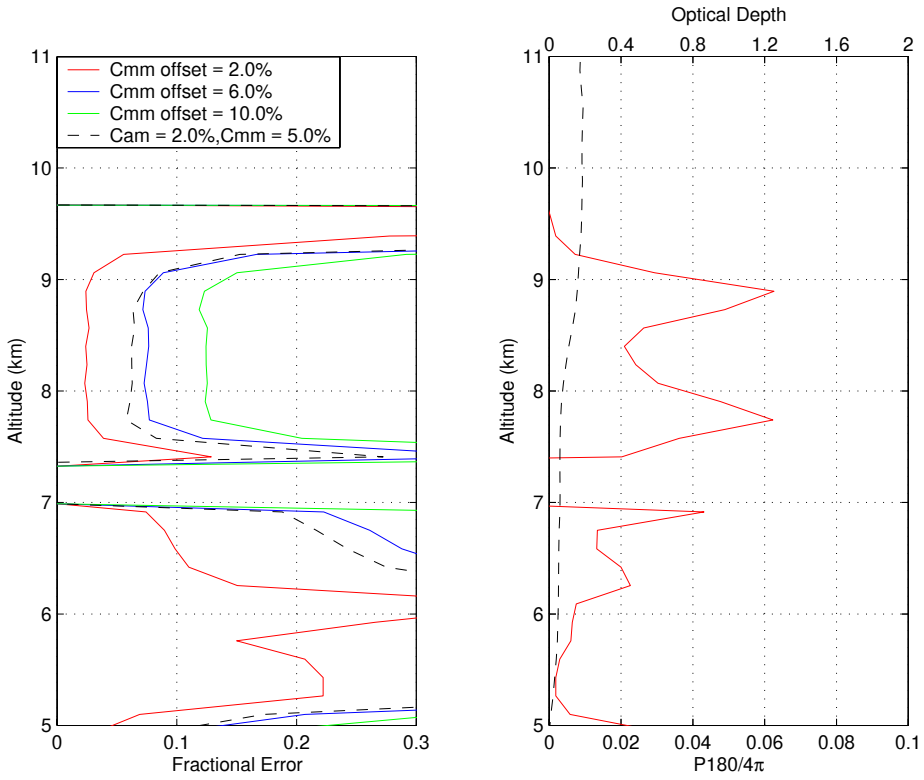

Figure 5-8, The HSRL measured backscatter phase function and optical depth profile is presented in the right plot for Feb-22, 2001. The axis representing the optical depth and backscatter phase function is located at the top and bottom of the figure respectively. The fractional change in the backscatter scatter phase function due varying differences in the off set of the calibration coefficient Cmm is presented as a function of range in the left profile. The dashed error profile is the fractional change in the backscatter phase function with a 2% offset in Cam and a 5% offset in Cmm.

5.6 Multiple Scatter Errors

The multiple scattering contributions can cause significant errors in the HSRL measurements. The single scatter lidar equation assumes that when a photon is scattered it is removed from the beam. In reality, up to half the total scattered energy is forward scattered, some of which remains in the receiver field of view and contributes to the lidar signal.

As discussed in chapter 3.2.2, multiple scattering has the largest impact when there is a large change in the extinction, such as cloud boundaries. To investigate the effectiveness of the aerosol backscatter cross-section non-uniformity filter, the data is filtered using varying tolerances for the non-uniformity filter ranging from 10% - 40% in Figure 5-9. In addition to the selected data points, the data that was rejected because of this filter was recorded according to whether the backscatter cross-section slope is positive or negative. The figure shows that data rejected by the non-uniformity criteria and with a positive slope have a distribution that peaks at larger backscatter phase function values compared to the selected distribution. In contrast, data that was rejected by a negative slope in the threshold criteria has a distribution shifted to smaller backscatter phase function values. The result is consistent with the expected behavior of the backscatter phase function due to multiple scattering as discussed in chapter 3.2.2.

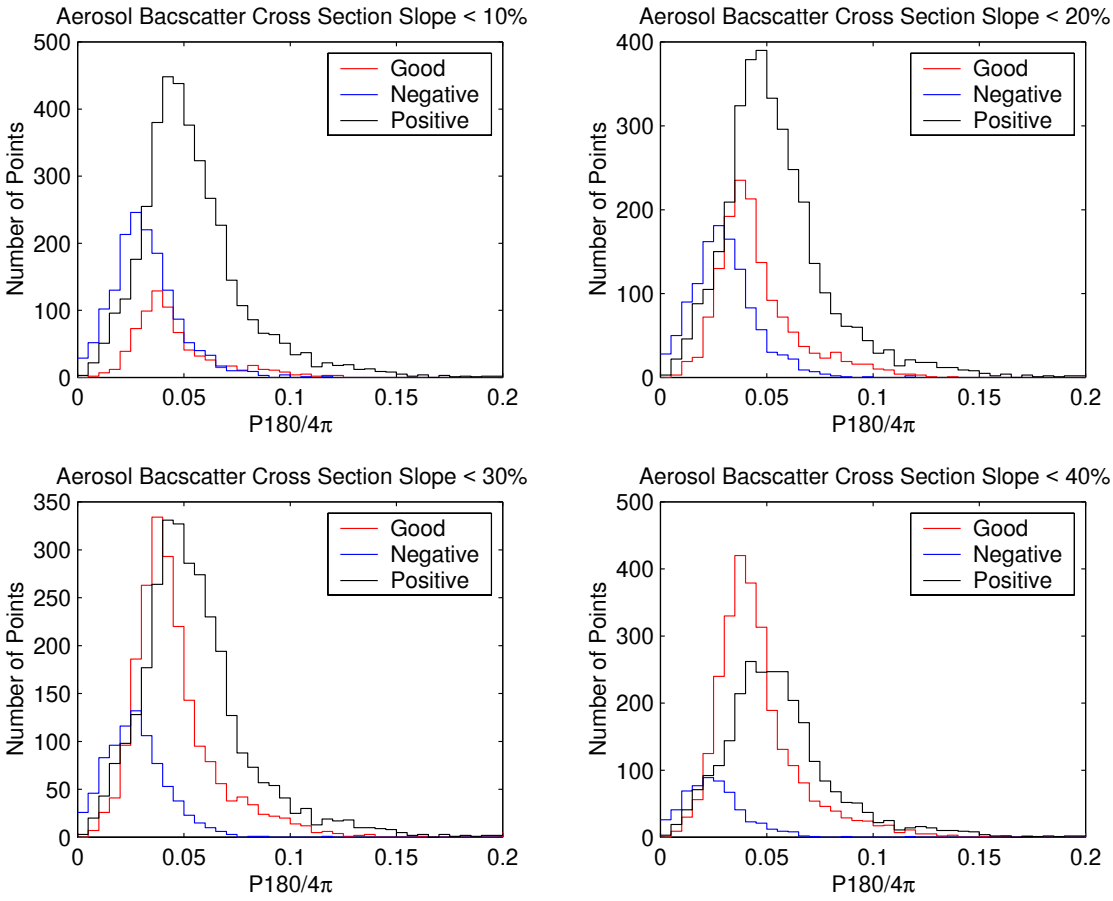

Figure 5-9, The backscatter phase function distribution using varying non-uniformity threshold criteria. The red distributions are data points that meet the criteria and have depolarization's > 25% and backscatter phase function random errors < 40%. The blue distributions are data points that meet the depolarization and random error criteria but exceed the non-uniformity threshold with a negative slope. The black distribution exceed the non-uniformity threshold but with a positive slope.

Chapter 6

6 Multiple Scatter Correction of HSRL Data

6.1 Introduction

To further investigate the effects of multiple scattering a multiple scatter model developed by (Eloranta, 1998) is used to correct for the multiple scatter contribution. This model can be applied to select cases where the cloud is uniform and does not have cloud layers below or above the selected cloud. In this chapter, a description of the model is presented and a correction is applied to 21 profiles. The effect of the multiple scatter correction is then investigated.

6.2 The Multiple Scatter Model

The model requires as input the instrument receiver field of view ρ_r , laser divergence ρ_l , aerosol scattering cross-section $\beta_s(r)$, and the particle diameter of the scattering medium *d*. The scattering cross-section $\beta_s(r)$ is measured using the HSRL. The laser divergence, ρ_l and receiver field of view ρ_r are defined by the instrument specification.

6.3 Model Assumptions

To understand the strengths and limitations of the model it is important to present the assumptions used. There are three important assumptions:

1. Gaussian forward phase function
2. Isotropic backscatter phase function
3. Only one large angle scattering event

6.3.1 Gaussian Forward Scattering Phase Function

For atmospheric aerosol scattering at 532 nm the wavelength of the transmitted beam is many times smaller then the diameter of the scattering particles in cirrus, *d*. From diffraction theory, if the wavelength is small compared to the scattering medium, one half the scattered energy is contained in the forward diffraction peak. The angular width of the diffraction peak is proportional to the diameter of the scattering particles $\theta \sim \frac{\lambda}{d}$, where λ the wavelength of the laser, and *d* is the diameter of the scattering particles.

The energy distribution in the forward diffraction peak is assumed Gaussian. This approximation has been shown to be a good approximation to the true forward scatter phase function (Eloranta, 1998) and simplifies the mathematics in the model.

6.3.2 Isotropic Backscatter Phase Function

The multiple scattered photons have a wide angular distribution compared to the transmitted beam. The multiple scatter model assumes the backscatter phase function $\frac{P(\pi,r)}{4\pi}$ is isotropic near 180 deg. This approximation can produce errors because the real atmosphere $\frac{P_{n\pi}(r)}{P(\pi,r)}$ is not one for aerosol scattering.

The HSRL overcomes this limitation because the molecular and aerosol backscattered photons are measured separately. Using the molecular return the uncertainty is eliminated because the molecular backscatter phase function $\frac{P_{mol}(\pi,r)}{4\pi}$ is

calculated for an atmospheric density profile and is isotropic near 180 degrees based on Rayleigh scattering theory.

6.3.3 Only One Large Angle Scattering Event

The model assumes when a photon is scattered into the receiver field of view it has encountered only one large angle scattering event. Multiple forward scattered events are allowed in the model. It has been demonstrated using Monte Carlo simulations (Kuehn, 2001), (Eloranta, 1998) that this approximation does not induce large errors in the model.

6.4 The Multiples Scatter Model Applied to the Measurements

The multiple scatter model is used to correct the HSRL extinction measurements for multiple scattering. As discussed in section 3.2.2, multiple scattering has the largest impact near the cloud base.

The multiple scatter correction is applied as follows:

1. Compute the bulk backscatter phase function $\frac{\overline{P(\pi, r, r_o)}}{4\pi}$ for the selected profile by fitting the integrated backscatter cross-section which is insensitive to multiple scattering to the optical depth well above the top of the cloud where the energy in the forward diffraction peak is outside the receiver field of view.

2. Run the multiple scatter model using the bulk backscatter phase function with varying particle sizes. The bulk backscatter phase function is insensitive to multiple

scattering because it is calculated well above the top of the cloud where most of the forward scattered energy is out side of the field of view of the receiver.

3. Apply the correction to the profile for each particle size. A least squared fit between the multiple scatter corrected optical depth and the integrated backscatter cross-section is measured at the top of the cloud. The integrated backscatter cross-section is relatively insensitive to multiple scattering errors. The particle size resulting in the best fit is selected. Figure 6-1 shows the multiply scatter corrected simple optical depth for different particle sizes. Notice that too small a particle size results in the simple optical depth underestimated at the top of the cloud (the red profile in the figure). When the particle size is too small the multiple scatter contribution is underestimated. The result is the optical depth at the top of the cloud is underestimated because of the extra multiple scatter energy still in the receiver field of view. Particle size overestimation results in the optical depth being too large at the top of the cloud (green profile). The multiple scattered energy is overestimated in the field of view of the receiver. The result is too little molecular signal at the top of the cloud and the optical depth is over estimated. With the correct particle size the optical depth will have the closest fit to the integrated backscatter cross-section (blue line).

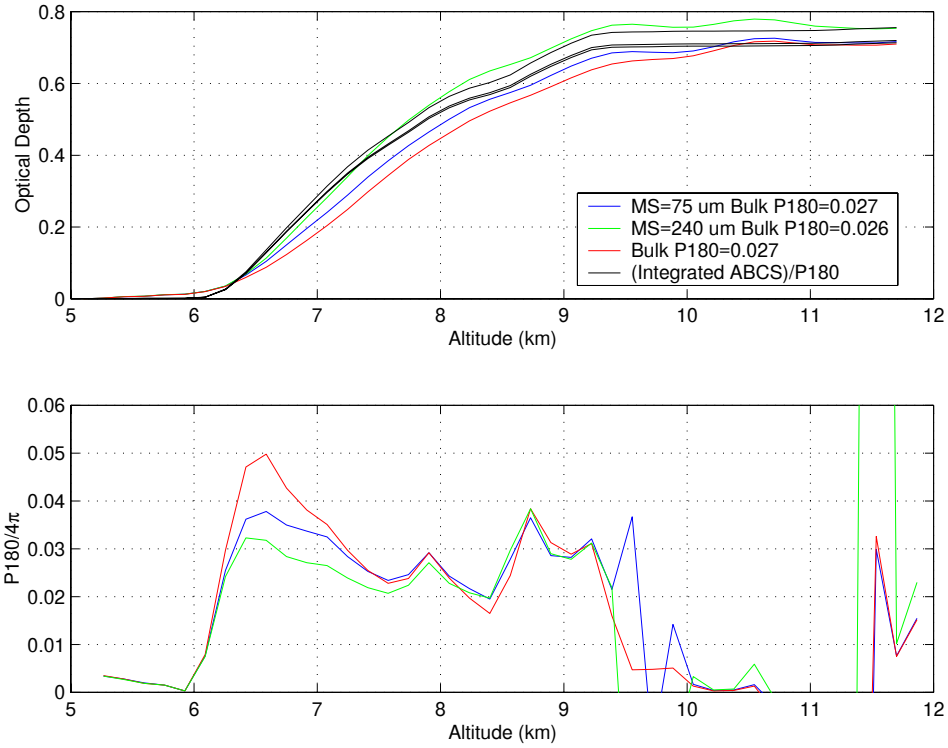

Figure 6-1, The top profile is the multiple scatter corrected optical depth shown with different particle sizes with the corresponding integrated backscatter cross-section (black lines). The backscatter phase functions computed using the same particle sizes in the top figure is presented in the bottom profile.

6.5 The Multiple Scatter Corrected Backscatter Phase Function Distribution

The multiple scatter correction was applied to 21 days that had uniform clouds. For each day the particle size was selected which minimized the least squared fit of the integrated backscatter cross-section and optical depth. The multiple scatter corrected backscatter phase function distribution is presented in Figure 6-2. The top distribution in Figure 6-2 shows the backscatter phase function values that have not been multiple scatter corrected. The distribution includes cloud edges where multiple scatter errors are large.

Notice the distribution has a peak value at ~0.04, the same location as Figure 3-3 which contains the entire data set but the multiple scatter corrected distribution is narrower. As discussed in section 3.2.2 the multiple scatter contribution will have the largest effect at the cloud base and cloud top. With the additional multiple scattering, a broader distribution would be expected. The multiple scatter correction should correct for these cases and one would expect the distribution to become narrower.

6.6 Validation Using Multiple Field of View Data

The multiple scatter correction was computed for February 22, 2001 and compared to a more robust calculation using multiple receiver fields of views (Kuehn, 2001). The particle size measured using the multiple field of view method was 75μm compared to 80μm using the method presented in this chapter.

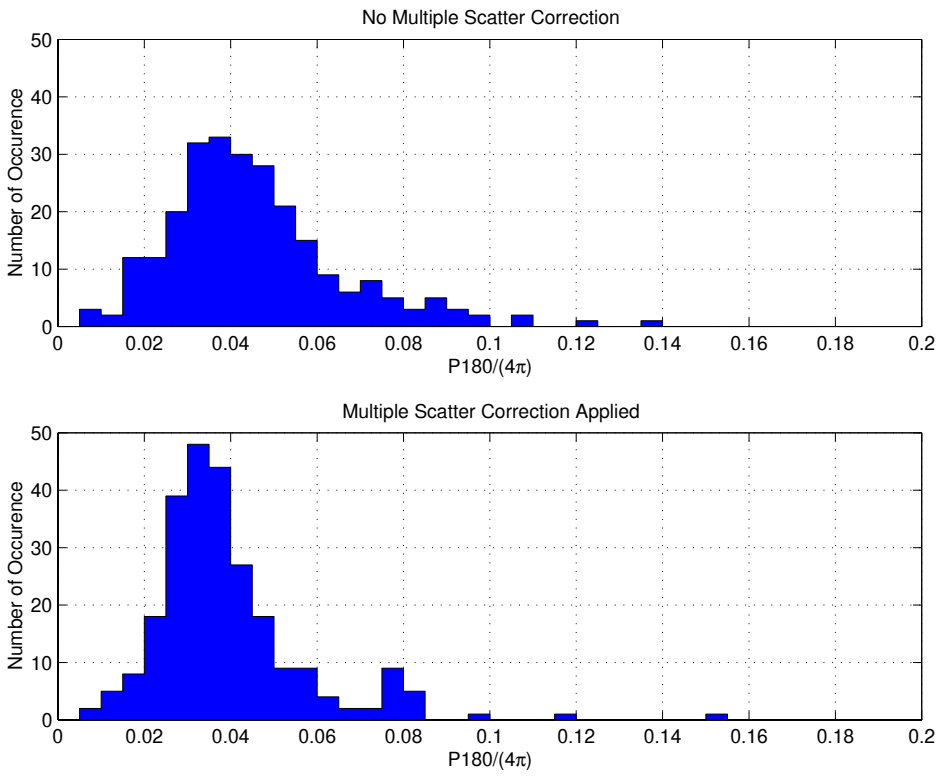

Figure 6-2, The multiple scatter corrected backscatter phase function distribution (bottom plot) and the uncorrected distribution (top plot) for 21 days. The data was filtered to eliminate points with scattering ratio errors > 2.0% and depolarization < 25%. Cloud edges are included in the distributions

6.7 The Multiple Scatter Correction Applied to a Single Profile

The multiple scatter correction is applied to a profile of the backscatter phase function in Figure 6-3. In this profile the uncorrected backscatter phase function has peak at the base of the cloud (8.5 km) that is approximately two times as large as the measured backscatter phase function in the middle of the cloud. The error bars are significantly smaller than the size of the peak which suggests that it is not a result of noise on the data. This peak is most likely not real, but instead an error caused by multiple scattering.

As discussed in chapter 3.2.2, at the base of the cloud half the scattered energy is forward scattered into the field of view of the receiver. The result is the measured extinction is half the actual value. With this error, the backscatter phase function is measured to be twice as large as the real value.

The multiple scatter corrected backscatter phase function profile is presented as the green profile in Figure 6-3. Notice the peak at the base of the cloud has been reduced by the multiple scatter correction. The correction did not significantly change the backscatter phase function in the middle of the cloud where the effect of multiple scattering is small. At the cloud top, the correction increased the backscatter phase function compared to the uncorrected profile. Even though the multiple scatter correction reduced the peak in the backscatter phase function at the cloud base, it is not clear that the multiple scatter correction is large enough at the base of the cloud. In future work a modified version of the multiple scatter model allowing a distribution of particle sizes will be applied. It is hoped that this will improve the correction.

Data that satisfies the aerosol backscatter cross-section non-uniformity threshold are presented with a blue circle in Figure 6-3. In this profile the threshold eliminates data near the cloud edge but does select data points near 7 km that could have multiple scatter errors.

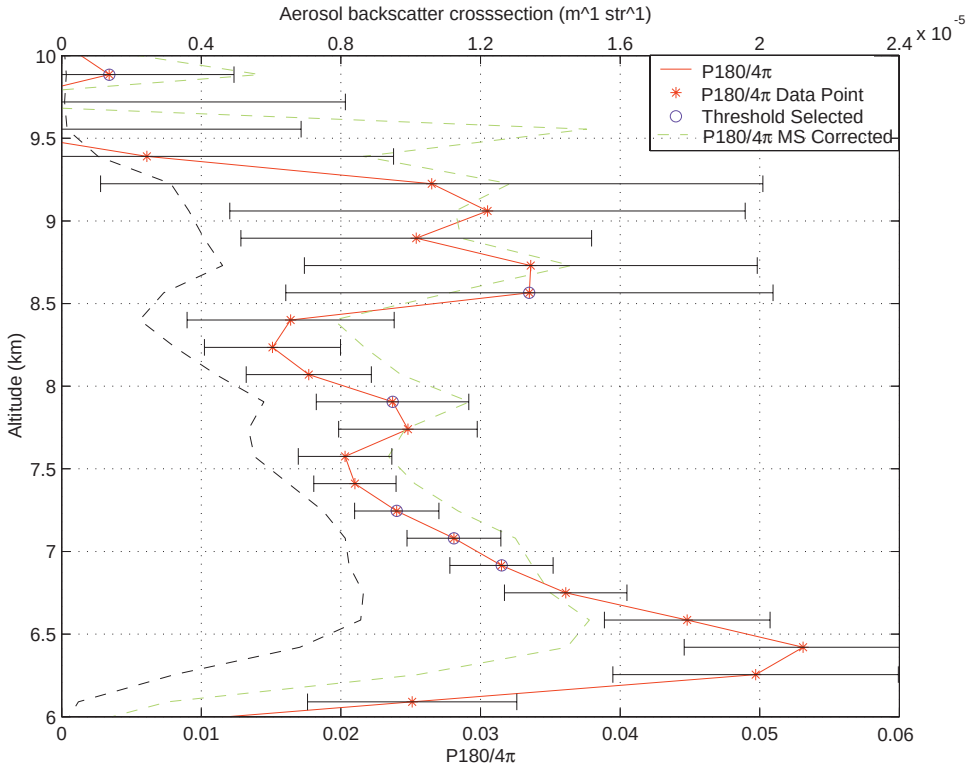

Figure 6-3, The multiple scatter corrected backscatter phase function (green profile) and the uncorrected backscatter phase function (red profile) with photon counting error bars from Feb-22, 2001. Data that satisfy the non-uniformity criteria are plotted with a blue circle. The aerosol backscatter cross-section is also included (black dashed profile).

6.8 Particle Size Measurements

A bulk particle size measurement results from the multiple scatter correction. Figure 6-4 plots the measured particle size versus temperature for the 21 selected days. Because of the limited number of days it difficult to make a definitive conclusion but the results suggests a positive correlation between particle size and temperature (Figure 6-4). This is in agreement with previous measurements that have demonstrated this correlation (Heymsfield, 1984).

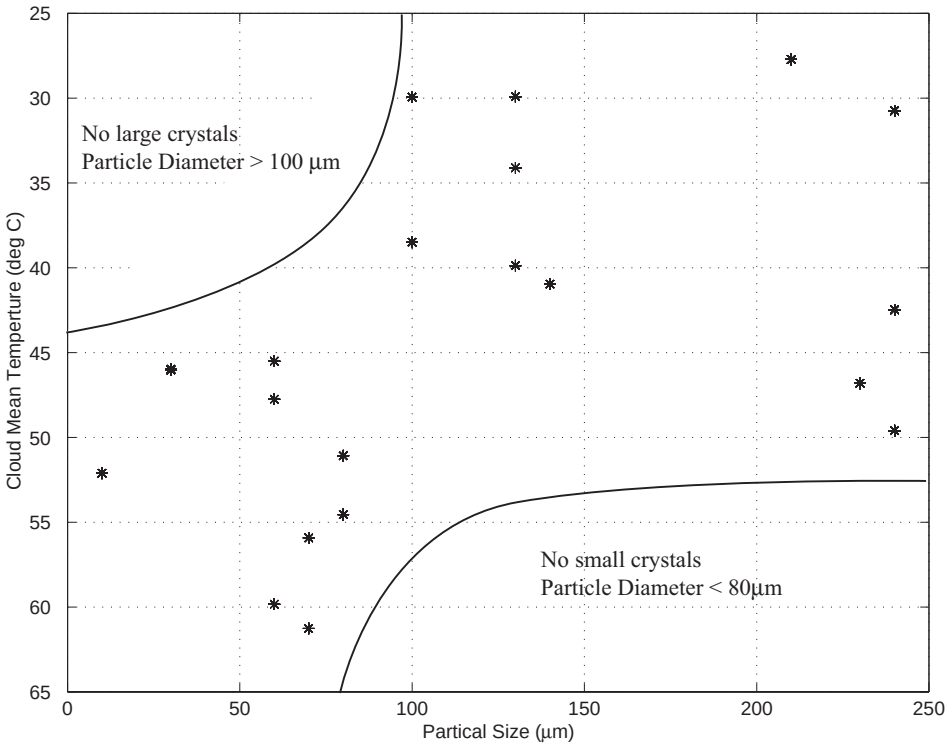

Figure 6-4, Particle size verse mean cloud temperature for the 21 multiple scatter corrected days. Notice that there are no crystals smaller then 100 μm with temperatures greater then -45 deg C and no large crystals (larger then 80 μm) at temperatures less then -50 deg C.

Chapter 7

7 Summary

In this thesis, measurements of the backscatter phase functions for 74 HSRL data sessions spanning over one year of data are presented. An important conclusion from this study is that the probability distribution of the measured backscatter phase functions of cirrus clouds have a discrete peak at $\frac{P180}{4\pi} \approx 0.04$. However, the results demonstrate that there can be large variability; values as large as 0.14 and as small as 0.005 are observed.

The results are supported by a rigorous error analysis including photon counting, systematic, and multiple scattering errors. It is demonstrated that photon counting and multiple scattering errors are most significant. Based on the analysis we are confident that the peak and the variability are real characteristics of cirrus and not an artifact of the measurement process. In fact, even when photon counting errors as large as 60% are included, the peak does not significantly change. However, despite significant effort to reduce multiple scattering effects including a small, 160μm field of view and removing measurements near cloud edges, the analysis suggests that the effect of multiple scattering has been reduced but not eliminated.

A multiple scatter correction was applied to 21 of the measurement profiles. The correction results in the narrowing of the backscatter phase function probability distribution with little effect on the location of the peak. Based on this result, the peak may be narrower than presented in this thesis.

The peaked distribution of the backscatter phase function is surprising considering wide variations of modeled backscatter phase functions for different crystal types. If cirrus ice crystal habit consisted of a wide range of pristine crystals, based on model calculations a peak in the backscatter phase function would not be expected. A predominant crystal type could explain the peak. However, with a single crystal type, only small variation in depolarization would occur. This was not found in the HSRL measurements near the peak. A more plausible explanation is the peak represents cases with irregular shaped crystals. The irregularity could result in a convergence of the backscatter phase function without depolarization dependence. The positive correlation of the backscatter phase function at large depolarization may represent cases of pristine crystals

The peak in the backscatter phase function is an important result for measurements of cloud optical depth using single channel lidars. Satellite based single channel lidars are expected to be completed in the near future, including GLAS and CALIPSO. These systems will offer global, high resolution measurements of the scattering properties of ice clouds. As discussed in this thesis, optical depth measurements using single channel lidars require knowledge of the relationship between the backscatter cross-section and extinction. The peak in the backscatter phase function found in the calibrated HSRL measurements suggests that using a backscatter phase function of 0.04 for single channel lidar optical depth retrievals will improve the accuracy of the optical depth measurements. The positive dependence of the backscatter phase function at large depolarization suggests that if depolarization information is available, varying the backscatter phase function as function of depolarization could improve the estimate of the backscatter phase function. However,

because a wide distribution of backscatter phase functions where found, using single value of the backscatter phase function for individual cases may result in large errors.

Currently, an autonomous HSRL is in development and is expected to be deployed at a site in Barrow Alaska in the spring of 2003. This system will offer continuous measurements of calibrated optical depth, aerosol backscatter cross-section, and backscatter phase functions measurements. Because the system will be operated on a continuous basis, a much larger and more robust data set of backscatter phase function measurements will be available.

References

Eloranta, E.W., 1998. Practical model for the calculation of multiply scattered lidar returns. Applied Optics, 37: 2464-2472.

Heymsfield, A.J.M., Karen M., 1990. The 27-28 October 1986 Fire IFO cirrus case study: cloud microstructure. Amercian Meteorological Society, 118 : 2313–2328.

Heymsfield, A.J.P., C.M.R, 1984. A parameterization of the particle size spectrum of ice clouds in terms of the ambient temperature and the ice water content. Journal of Atmospheric Sciences, 41 : 846-855.

Hughes, H.G.F., Jerry A.; Stephens,Donald H., 1985. Sensitivity of lidar inversion algorithm to parameters relating atmospheric backscatter and extinction. Applied Optics, 24 : 1609-1612.

Klett, J.D., 1981. Stable analytical inversion solution for processing lidar returns. Applied Optics, 20: 211-220.

Kuehn, R.E., 2001. A technique to measure cirrus cloud effective particle size using a high spectral resolution lidar

Macke, A.F., Peter N.; McFarquhar, Greg M.; Kinne, Stefan, 1998. The role of ice particle shapes and size distributions in the single scattering properties of cirrus clouds. Journal of Atmospheric Sciences, 55: 2874-2883.

Nelson, J., 1998. Sublimation of ice crystals. Journal of Atmospheric Sciences, 55: 910-919.

Piironen, P., 1994. A High Spectral Resolution Lidar based on an iodine absorption filter. PhD thesis, University of Joensuu, Department of Physics.

Sassen, K.C., Jennifer, M., 2001. A midlatitude cirrus cloud climatology from the facility for Atmospheric Remote Sensing. Part III: Radiative Properties. Journal of Atmospheric Sciences, 58: 2113-2127.

Spinehirne, J.D., 1995. Cirrus infrared parameters and shortwave reflectance relations from observations. Journal of Atmospheric Sciences, 53: 1438-1458.

Stephens, L.G.T., St-Chee; Stackhouse, Paul, W,JR..; Flatau, Piotr, 1990. The relevance of the microphysical and radiative properties of cirrus clouds to climate and climatic feedback. Journal of Atmospheric Sciences, 47: 1742–1754.

Wylie, D.P., 1994. Four years of global cirrus cloud statistics using HIRS. Journal of Climate, 7: 1972-1986.

Appendix A: Photon Counting Error Equations

List of Symbols

$N_a(r) = \frac{dN_a(r)}{dt}$ = Number of aerosol scattered photons incident on the receiver field of view

$N_m(r) = \frac{dN_a(r)}{dt}$ = Number of molecular scattered photons incident on the receiver field of view

$S_m(r) = \frac{dS_m(r)}{dt} r^2$ = Range corrected signal measured in the molecular channel

$S_{a+m}(r) = \frac{dS_{a+m}(r)}{dt} r^2$ = Range corrected signal measured in the combined channel

dt = 100 ns range bin (15 meters)

C_{am} = The fraction of the aerosol signal in the molecular channel relative to the aerosol signal in the combined channel

$C_{mm}(r)$ = The fraction of the molecular signal detected in the molecular channel relative to the molecular signal in the aerosol channel

$B_{a+m}(r)r^2$ = The range corrected backround signal measured in the combined channel

$B_m(r)r^2$ = The range corrected backround signal measured in the molecular channel

$\beta_m(r)$ = The molecular backscatter cross-section computed from an atmospheric temperature profile

η = System efficiency of the combined channel

σ = standard deviation

Separated molecular and aerosol returns

$$N_m(r) = \frac{\frac{S_m(r) - B_m}{r^2}_m - C_{am}\left(\frac{S_{a+m}(r)}{r^2} - \frac{B_{a+m}}{r^2}\right)}{\eta\left(C_{mm}(r) - C_{am}\right)}$$

$$N_a(r) = \frac{\frac{S_{a+m} - B_{a+m}}{r^2}}{\eta} - \left(\frac{-C_{am}\frac{S_{a+m}(r) - B_{a+m}}{r^2} + \frac{S_m(r) - B_m}{r^2}}{\eta\left(-C_{am} + C_{mm}(r)\right)} \right)$$

The backscatter cross-section

$$\beta_a(r)\frac{P_a(\pi,r)}{4\pi}=\frac{3}{8\pi}\frac{\beta_m(r)\left(-C_{am}+C_{mm}(r)\right)\left(S_{a+m}(r)-B_{a+m}\right)-\frac{-C_{am}\left(S_{a+m}(r)-Sb_{a+m}\right)+S_m(r)-B_m}{\left(-C_{am}+C_{mm}(r)\right)}}{-C_{am}\left(S_{a+m}(r)-B_{a+m}\right)+S_m(r)-B_m}$$

The partial derivatives are:

$$\frac{\partial\beta_a(r)\frac{P_a(\pi,r)}{4\pi}}{\partial S_m}=-\frac{3}{8\pi}\frac{\beta_m(r)\left(-C_{am}+C_{mm}(r)\right)\left(S_{a+m}(r)-B_{a+m}-\frac{-C_{am}\left(S_{a+m}(r)-B_{a+m}\right)+S_m(r)-B_m}{\left(-C_{am}+C_{mm}(r)\right)}\right)}{\left(-C_{am}(S_{a+m}(r)-B_{a+m})+S_m(r)-B_m\right)^2}-$$

$$\frac{3}{8\pi}\frac{\beta_m(r)}{\left(-C_{am}(S_{a+m}(r)-B_{a+m})+S_m(r)-B_m\right)}$$

$$\frac{\partial\beta_a(r)\frac{P_a(\pi,r)}{4\pi}}{\partial S_{a+m}}=\frac{3}{8\pi}\frac{\beta_m(r)C_{am}\left(-C_{am}+C_{mm}(r)\right)\left(S_{a+m}(r)-B_{a+m}-\frac{-C_{am}\left(S_{a+m}(r)-B_{a+m}\right)+S_m(r)-B_m}{\left(-C_{am}+C_{mm}(r)\right)}\right)}{\left(-C_{am}(S_{a+m}(r)-B_{a+m})+S_m(r)-B_m\right)^2}+$$

$$\frac{3}{8\pi}\frac{\beta_m(r)(-C_{am}+C_{mm}(r))\left(1+\frac{C_{am}}{-C_{am}+C_{mm}(r)}\right)}{\left(-C_{am}(S_{a+m}(r)-B_{a+m})+S_m(r)-B_m\right)}$$

$$\frac{\partial\beta_a(r)\frac{P_a(\pi,r)}{4\pi}}{\partial B_{a+m}}=-\frac{3}{8\pi}\frac{\beta_m(r)C_{am}\left(-C_{am}+C_{mm}(r)\right)\left(S_{a+m}(r)-B_{a+m}-\frac{-C_{am}S_{a+m}(r)-B_{a+m}+S_m(r)-B_m}{\left(-C_{am}+C_{mm}(r)\right)}\right)}{\left(-C_{am}(S_{a+m}(r)-B_{a+m})+S_m(r)-B_m\right)^2}+$$

$$\frac{3}{8\pi}\frac{\beta_m(r)(-C_{am}+C_{mm}(r))\left(-\frac{C_{am}}{-C_{am}+C_{mm}(r)}-1\right)}{\left(-C_{am}(S_{a+m}(r)-B_{a+m})+S_m(r)-B_m\right)}$$

$$\frac{\partial\beta_a(r)\frac{P_a(\pi,r)}{4\pi}}{\partial B_m}=\frac{3}{8\pi}\frac{\beta_m(r)\left(-C_{am}+C_{mm}(r)\right)\left(S_{a+m}(r)-B_{a+m}-\frac{-C_{am}(S_{a+m}(r)-B_{a+m})+S_m(r)-B_m}{-C_{am}+C_{mm}}\right)}{\left(-C_{am}(S_{a+m}(r)-B_{a+m})+S_m(r)-B_m\right)^2}+$$

$$\frac{3}{8\pi}\frac{\beta_m(r)C_{am}}{-C_{am}(S_{a+m}(r)-B_{a+m})+S_m(r)-B_m}$$

$$\frac{\partial\beta_a(r)\frac{P_a(\pi,r)}{4\pi}}{\partial\beta_m}=\frac{3}{8\pi}\frac{\left(-C_{am}+C_{mm}(r)\right)\left(S_{a+m}(r)-B_{a+m}-\frac{-C_{am}(S_{a+m}(r)-B_{a+m})+S_m(r)-B_m}{-C_{am}+C_{mm}(r)}\right)}{-C_{am}(S_{a+m}(r)-B_{a+m})+S_m(r)-B_m}$$

The backscatter cross-section photon counting errors are:

$$\sigma^2_{\beta_a(r)\frac{P_a(\pi,r)}{4\pi}} = \left(\frac{\partial\beta_a \frac{P_a(\pi,r)}{4\pi}(r)}{\partial S_{a+m}(r)}\right)^2 \sigma^2_{S_{a+m}}(r) + \left(\frac{\partial\beta_a \frac{P_a(\pi,r)}{4\pi}(r)}{\partial S_m(r)}\right)^2 \sigma^2_{S_m}(r) + \left(\frac{\partial\beta_a \frac{P_a(\pi,r)}{4\pi}(r)}{\partial B_m(r)}\right)^2 \sigma^2_{B_{a+m}}(r) +$$

$$\left(\frac{\partial\beta_a(r)\frac{P_a(\pi,r)}{4\pi}}{\partial B_{a+m}(r)}\right)^2 \sigma^2_{B_{a+m}}(r) + \left(\frac{\partial\beta_a(r)\frac{P_a(\pi,r)}{4\pi}}{\partial\beta_m(r)}\right)\sigma^2\beta_m(r)$$

The Optical Depth

$$\mathrm{OD}(\mathrm{r_o}) = \tau(r) - \tau(r_o) = -\frac{1}{2}\ln\left[\frac{-C_{am}(-S_{a+m} - B_{a+m}) + S_m - B_m}{\beta_m(r)(C_{mm} - C_{am})Scl(r_o)}\right]$$

Where: Scl(r_o) = Scale factor to normalize the optical depth at r_o
In this thesis the optical depth is normalized to zero at 5 km.

The partial derivatives are:

$$\frac{\partial OD(r)}{\partial S_m(r)} = -\frac{1}{2\left(-C_{am}\left(C_{a+m}(r) - B_{a+m}(r)\right) + S_m(r) - B_m(r)\right)}$$

$$\frac{\partial OD(r)}{\partial S_{a+m}(r)} = \frac{C_{am}}{2\left(-C_{am}\left(S_{a+m}(r) - B_{a+m}\right) + S_m(r) - B_m(r)\right)}$$

$$\frac{\partial OD(r)}{\partial \beta_m(r)} = \frac{1}{2\beta_m(r)}$$

$$\frac{\partial OD(r)}{\partial B_m(r)} = \frac{1}{2\left(-C_{am}\left(S_{a+m}(r) - B_{a+m}(r)\right) + S_m(r) - B_m(r)\right)}$$

$$\frac{\partial OD(r)}{\partial B_{a+m}(r)} = -\frac{C_{am}}{2\left(-C_{am}\left(S_{a+m}(r) - B_{a+m}\right) + S_m(r) - B_m\right)}$$

The optical depth photon counting errors is:

$$\sigma^2{}_{OD(r)} = \left(\frac{\partial OD(r)}{\partial S_{a+m}(r)}\right)^2 \sigma^2{}_{S_{a+m}}(r) + \left(\frac{\partial OD(r)}{\partial S_m(r)}\right)^2 \sigma^2{}_{S_m}(r) + \left(\frac{\partial OD(r)}{\partial B_m(r)}\right)^2 \sigma^2{}_{B_{a+m}}(r) + \left(\frac{\partial OD(r)}{\partial B_{a+m}(r)}\right)^2 \sigma^2{}_{B_{a+m}}(r) + \left(\frac{\partial OD(r)}{\partial \beta_m(r)}\right) \sigma^2{}_{\beta_m}(r)$$

Extinction cross-section

The extinction cross-section averaged between points r_2 and r_1 are:

$$\langle \beta_e(r_2, r_1) \rangle = \frac{OD(r_2) - OD(r_1)}{r_2 - r_1}$$

In this thesis the extinction is measured across 11 bins or 165 meters.

The error in the extinction is:

$$\sigma^2{}_{\beta_e}(r) = \frac{\sigma^2{}_{OD(r2)} + \sigma^2{}_{OD(r_1)}}{(r_2 - r_1)^2}$$

The backscatter phase function

The backscatter phase function is:

$$\frac{P_a(\pi, r)}{4\pi} = \frac{\beta_a(r) \frac{P_a(\pi, r)}{4\pi}}{\beta_e(r)}$$

The backscatter phase function partial derivatives are:

$$\frac{\partial \frac{P_a(\pi,r)}{4\pi}(r)}{\partial \beta_a(r) \frac{P_a(\pi,r)}{4\pi}(r)} = \frac{1}{\beta_e(r)}$$

$$\frac{\partial \frac{P_a(\pi,r)}{4\pi}(r)}{\partial \beta_e(r)} = -\frac{\beta_a(r) \frac{P_a(\pi,r)}{4\pi}}{\left(\beta_e(r)\right)^2}$$

The backscatter phase function photon counting error is:

$$\sigma^2_{\frac{P_a(\pi,r)}{4\pi}}(r) = \left(\frac{\partial \frac{P_a(\pi,r)}{4\pi}}{\partial \beta_{\beta_a(r)\frac{P_a(\pi,r)}{4\pi}}}(r) \right)^2 \sigma^2_{\beta_{\beta_a(r)\frac{P_a(\pi,r)}{4\pi}}}(r) + \left(\frac{\partial \frac{P_a(\pi,r)}{4\pi}}{\partial \beta_e}(r) \right)^2 \sigma^2_{\beta_e}(r)$$